

## RESEARCH ARTICLE

10.1002/2017JC013089

## Key Points:

- Model results suggest that years with both strong upwelling and an intense California Undercurrent result in the lowest DO in slope bottom waters
- The long-term trend toward declining shelf bottom water DO in the NCCS is associated with both large-scale advection and local biogeochemical processes

## Correspondence to:

S. M. Durski,  
sdurski@coas.oregonstate.edu

## Citation:

Durski, S. M., J. A. Barth, J. C. McWilliams, H. Frenzel, and C. Deutsch (2017), The influence of variable slope-water characteristics on dissolved oxygen levels in the northern California Current System, *J. Geophys. Res. Oceans*, 122, 7674–7697, doi:10.1002/2017JC013089.

Received 11 MAY 2017

Accepted 16 AUG 2017

Accepted article online 25 AUG 2017

Published online 21 SEP 2017

Corrected 20 NOV 2017 and

Corrected 13 AUG 2018

This article was corrected on 20 NOV 2017 and 13 AUG 2018. See the end of the full text for details.

## The influence of variable slope-water characteristics on dissolved oxygen levels in the northern California Current System

Scott M. Durski<sup>1</sup> , John A. Barth<sup>1</sup>, James C. McWilliams<sup>2</sup>, Hartmut Frenzel<sup>3</sup> , and Curtis Deutsch<sup>3</sup> 
<sup>1</sup>College of Earth, Ocean and Atmospheric Sciences, Oregon State University, Corvallis, Oregon, USA, <sup>2</sup>Department of Atmospheric and Oceanic Sciences, University of California, Los Angeles, California, USA, <sup>3</sup>School of Oceanography, University of Washington, Seattle, Washington, USA

**Abstract** Observations have suggested a trend of decreasing dissolved oxygen (DO) and increasing spiciness in summertime middepth slope waters and bottom shelf waters along the United States west coast over the past 50 years, but they have also demonstrated a large amount of interannual and decadal variability. Shelf bottom water and slope water properties can be influenced by both local and remote effects, including changes in circulation or changes in the characteristics of the source waters supplying the region. A regional-scale, coupled physical biogeochemical model has been developed to simulate seasonal-to-decadal scale variability along the US west coast to discern the physical dynamics behind these spatial and temporal patterns. A simulation run from 1981 to 2006 with forcing that incorporates the larger scale interannual trends reproduces the development of low DO late in the upwelling season, the considerable interannual variability and the reported tendency toward a shoaling, more spicy, and oxygen-depleted, northern California Undercurrent (CU). Whereas the trend in spiciness in the model results from increased influence of equatorial relative to subarctic source waters, the decreases in DO are found to additionally be a consequence of local biogeochemical processes. In order to better understand the interannual variability, years of the simulation were classified into four groups based on intensity of upwelling forcing and undercurrent strength. Slope water characteristics, shelf-slope exchange, and slope-basin exchange were compared across the four cases. Years with both strong upwelling and a strong undercurrent generated the most negative anomalies in slope-water DO late in the upwelling season.

**Plain Language Summary** During the summertime, dissolved oxygen(DO) concentrations in coastal bottom waters sometimes decline to levels that stress a variety of the native organisms. These declines can be associated with local processes, such as enhanced respiration when the overlying waters are highly productive or remote influences such as the circulation of low DO water into these regions. The ‘source waters’, that are typically transported into the coastal region along the bottom, originate off the continental shelf, on the continental slope. Here we study the role of the slope water in altering the characteristics of the coastal bottom water by using a model simulation of both physical circulation and the principal biological processes. The model simulates the period 1981–2006. We explore how trends in the characteristics of the slope water correlate with trends in the coastal waters and what physical phenomena are associated with the strongest DO declines in coastal bottom water. We find that years that have both high productivity due to upwelling of nutrient rich water onto the shelf and a strong northward flowing undercurrent along the continental slope tend to have the most negative impact.

## 1. Introduction

Measurements of the coastal shelf waters of the western North Pacific have become increasingly abundant in recent years, thanks to both remote sensing and directed field programs. But observations of the main thermocline of the adjacent continental slope waters remain sparse. In this study, we apply a multidecadal regional simulation of an eddy-resolving coupled physical-biogeochemical model together with available observations to learn about the characteristics, trends, variability, and dynamics of this intermediate layer

along the continental margin with a particular focus on DO. These subsurface waters represent both the main source waters for the highly productive upwelling season as well as a potential export pathway for shelf particulate matter [Hales *et al.*, 2006].

The predominant dynamical feature on the slope is the California Undercurrent (CU). This current, typically found at depths between  $-500$  and  $-150$  m (densities between  $\sigma_\theta = 26.4\text{--}26.6$  kg m $^{-3}$ ) transports warm, salty, lower oxygen water poleward, and has been measured as far south as Baja California and as far north as Vancouver Island [Huyer *et al.*, 1998]. The width of the current scales with the Rossby radius of deformation but is also affected by bathymetric features such as submarine canyons [Thomson and Krassovski, 2010]. Maximum current speeds in the undercurrent can have been measured to reach  $0.2$  m s $^{-1}$  [Pierce *et al.*, 2000] but vary significantly spatially and temporally. Seasonally, the maximum poleward velocities develop in late summer, and minimum velocities occur in late spring [Chelton, 1984; Thomson and Krassovski, 2010]. During the summer upwelling season, the CU is a fully submerged feature, flowing in a direction opposite to that of the equatorward surface upwelling jet, but with the reversal of the predominant wind direction in the fall and winter, the CU merges with the surface Davidson Current. Connolly *et al.* [2014] in a model analysis of the northern portion of the undercurrent, found that it resulted from both barotropic and baroclinic alongshore pressure gradients associated with local and remote wind forcing and poleward propagating sea surface height variability. As the current flows northward, it is found to lose energy and exchange properties with the surrounding waters through the shedding of anticyclonic eddies [Pelland *et al.*, 2013].

Thus, slope water in the northern California Current System (NCCS, specified here as the portion of the California Current System north of  $42^\circ\text{N}$ ) is generally considered to be a mixture of northern and southern end member water masses. The southern source water is Pacific equatorial water (PEW) that is transported northward in the undercurrent which gradually mixes with Pacific subarctic upper water (PSUW) that enters the California current system from the North.

Long-term changes in the characteristics of these source waters and the resulting slope water have been documented in a number of studies in the past 10 years. Some of the earlier studies were regional and/or focused on several decades of observations, while more recent studies have been more comprehensive, encompassing larger temporal and spatial scales. Earlier regional studies reported a trend of decreasing DO on interdecadal time scales in the southern California Current System [Bograd *et al.*, 2008; McClatchie *et al.*, 2010] in the NCCS [Pierce *et al.*, 2012] and at Ocean Station Papa [Whitney *et al.*, 2007]. More recent studies which aggregated data from larger swaths of the west coast and for, in some cases, longer periods of time have found that the trend may be one phase in a pattern of interdecadal variability. Meiville and Johnson [2013] and Crawford and Peña [2013] both found the trend of declining DO to be robust roughly from 1980 to 2012, but suggested no trend of possibly increasing DO prior to 1980. Crawford and Peña [2016], in a comprehensive reevaluation of observations back to 1950 noted that intermediate depth oxygen levels on the continental slope peaked around 1980, gradually increasing prior and decreasing since. Pozo Buil and Di Lorenzo [2017] found that the decadal scale variability in subsurface salinity, and by association DO, over the past 60 years, at the larger scale of the CCS, could be anticipated by tracking anomalies along the path of the North Pacific Current, but did not draw conclusions about the narrow CUC.

Regardless of whether the historical patterns resolve into linear trends, oscillations or complex variability periods of decline in slope water DO have the potential for negative ecological consequences [McClatchie *et al.*, 2010; Deutsch *et al.*, 2011] and a better understanding of the interplay between the large-scale influences on slope water characteristics with regional processes is essential to explaining occurrences of coastal hypoxia. For example, Nam *et al.* [2015], find that for the Southern California Bight, roughly only 50% of the change in DO concentration of the CU can be explained as a change in source water properties. The northern portion of the system (roughly off the coast of northern California to British Columbia) is likely to differ as summer upwelling winds tend to be weaker than those to the south and winter downwelling winds tend to be stronger.

This study examines the results from a 26 year eddy-resolving coupled physical-biogeochemical regional model of the California current system during a period of declining DO (1980–2006) to learn the trends in slope water properties, gain insights into undercurrent variability on interannual time scales, and explore shelf/slope and slope/basin exchanges, focusing particularly on the NCCS. The model is an evolutionary

extension of previous California current simulations by *Marchesiello et al.* [2003] and *Gruber et al.* [2006] that includes the Biogeochemical Elemental Cycling (BEC) model [Moore et al., 2004]. Section 2 gives a brief description of the numerical model setup. Section 3 presents validation of the model with observations. In section 4, the modeled slope water characteristics and long-term linear trends are examined. In sections 5, each year of simulation is classified based on the intensity of upwelling wind forcing in the NCCS and the strength of the undercurrent (over the upwelling season). This is then used to compare and contrast the influence of the slope waters on the shelf and the adjacent basin as a function of upwelling and undercurrent strength.

## 2. Model Setup

Model simulations are run for the period from January 1981 to December 2006. For this, the Regional Ocean Modeling System [Shchepetkin and McWilliams, 2005] is configured for a domain that extends along the United States west coast from 30°N to 49°N, and stretches offshore approximately 1400 km. A curvilinear grid is used in the horizontal with close to uniform 5 km horizontal resolution and 33 vertical  $s$  coordinate levels. Atmospheric forcing is obtained from the North American Regional Reanalysis [Mesinger et al., 2006], using 5 day averaged fields. Boundary conditions for  $u$ ,  $v$ ,  $T$ , and  $S$  are constructed from the Simple Ocean Data Assimilation system [Carton et al., 2005] from 5 day averaged fields.

As mentioned above the ecosystem model implementation follows Moore et al. [2004]. It includes multiple phytoplankton functional groups (small phytoplankton, diatoms, calcifiers, and diazotrophs) subject to multiple limiting nutrients (nitrate, ammonium, phosphate, iron, and silicate) and iron cycling (including surface deposition and sediment efflux) and grazing by a single zooplankton. The sinking detrital pool is partitioned into fast and slow sinking components following the mineral ballast model of Armstrong et al. [2002]. Material reaching the seafloor is instantaneously remineralized to  $\text{NH}_4$ ,  $\text{PO}_4$ , dissolved inorganic carbon (DIC), Alkalinity (Alk),  $\text{SiO}_3$ , and Fe. Boundary conditions for biogeochemical fields are derived from monthly climatology, repeated over each year of the simulation. Nutrients and DO are obtained from the World Ocean Atlas [Garcia et al., 2010a, 2010b]. DIC and Alk are from GLODAP [Key et al., 2004]. A 10 year spin-up with monthly climatologies for forcing and boundary conditions was performed before the hindcast simulation. Monthly average output from the 26 year simulation is analyzed in this study.

## 3. Model Validation

Slope water characteristics are generally determined by mixing of water masses advected into the region from the north and south. So as a preliminary verification of the utility of this model the spatial  $T$  and  $S$  structure over the domain is compared with observations. Data on the vertical structure of the water column within the model domain is available from 3644 Argo profiles obtained between April 2001 and the end of the model simulation in December 2006 [Argo, 2000]. A direct point-by-point comparison is not informative because a large portion of the domain is eddy-dominated. But a basic statistical comparison demonstrates that the model captures the mean and variability in the density structure and stratification relatively well (Figure 1a). The upper 200 m of the water column has a positive deviation from the observations in density and spice ( $\Pi$ ) (Figures 1a and 1c) indicating that the model tends to overestimate upper thermocline and surface salinity offshore. This may result from inadequate representation of inflow of relatively lower salinity subarctic waters through the northwestern open boundary. The subsurface minimum in  $\Pi$  (and salt) at 150 m depth is largely lacking leading to an underestimate of stratification (Figure 1b) in the model between 250 and 100 m depth.

Although the end-member water characteristics in the model (Figure 1e) differ somewhat from Argo estimates, they present fair representations of two distinctly different water types that enter the domain from the north and south. At a given density, the northern water is fresher, cooler, and less spicy than the comparable southern water. Spiciness decreases with decreasing density for the northern water, while it generally increases with decreasing density for the southern end-member.

In addition to having a reasonable representation of  $T$ - $S$  structure offshore, it is important that the model exhibit reasonable seasonal variability on the shelf as coastal upwelling and downwelling circulations significantly influence the slope over much of the year. We compare the simulation output with observational

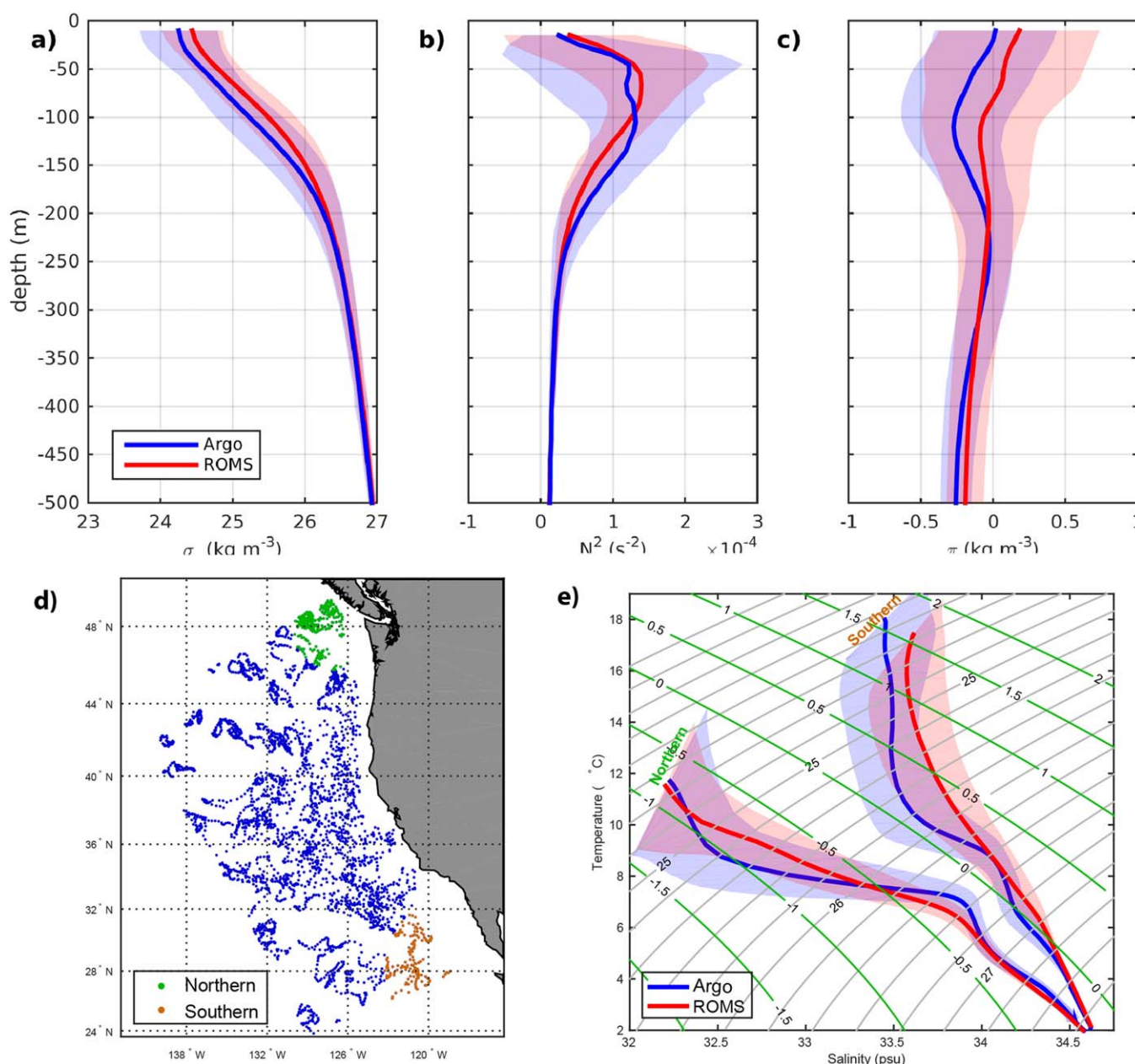


**Figure 1.** Mean profiles of (a) sigma-theta, (b) buoyancy frequency, and (c) spiciness from Argo profiles and the model along with a T-S diagram. Argo data averaged in plots (a–c) is from all float profiles within the domain between April 2001 and the end of the simulation (displayed as dots in Figure 1d)). Model fields are interpolated to the profile positions in time and space. Red and blue shaded regions indicate  $\pm 1$  SD from the mean for the floats and the model data, respectively. Argo and model data is averaged over a subset of Argo profile locations representing northern-origin (green dots in Figure 1d) and southern-origin (orange dots in Figure 1d) waters in Figure 1e.

data sets of temperature, salinity, and northward velocity at a shelf mooring. The mooring (NH-10), located approximately 20 km off Newport Oregon in 80 m of water, recorded temperature and salinity between 2000 and 2005, and currents from 1997 to 2004. The monthly averaged simulation output captures the seasonal cycle in low-pass filtered (30 day) observational fields relatively well (Figure 2). The seasonal cycle in atmospheric forcing leads to circulation on the Oregon shelf being predominantly associated with northward alongshore jets, during the downwelling winter season (November–March), and southward during the upwelling summer season (April–October). The seasonal patterns in temperature and salinity are well matched other than a tendency to overestimate midwater column temperatures early in the upwelling season and overestimate salinity in the second half of the year (perhaps due to a lack of rivers in the model).



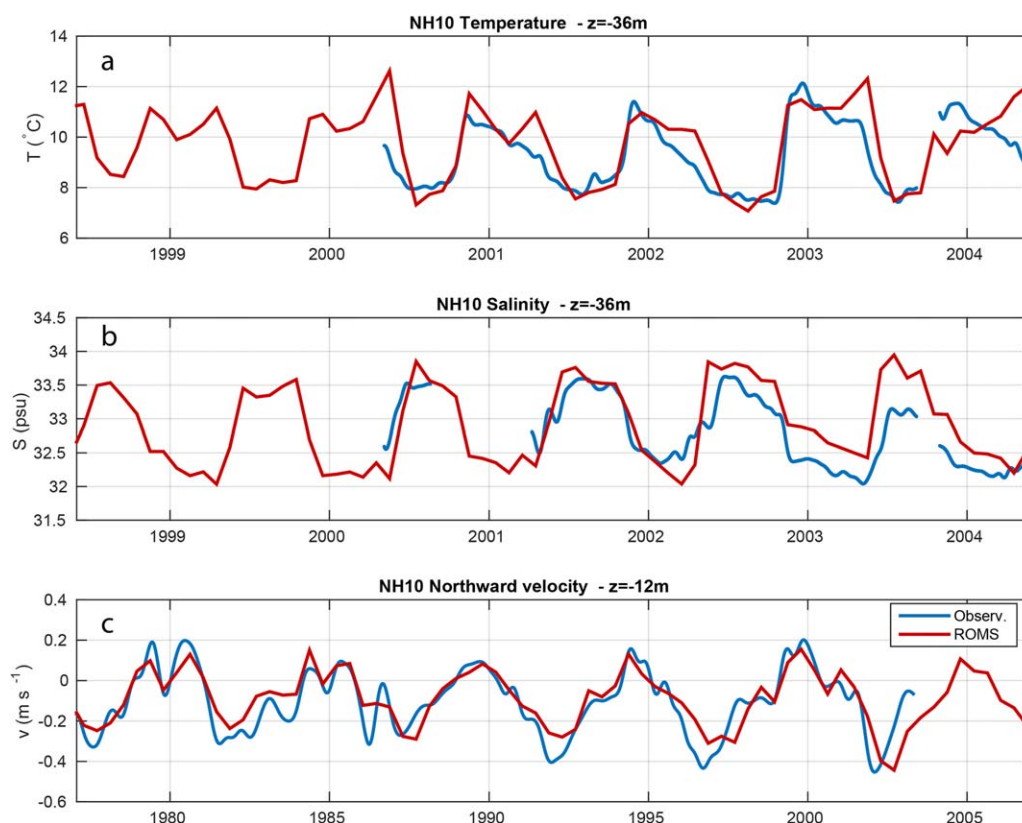


**Figure 2.** Comparison of low-pass filtered (30 day). (a) Temperature, (b) salinity, and (c) northward current velocity from the NH-10 mooring on the Oregon Shelf with monthly averaged simulation output.

While the smoothness of the bathymetry representing Heceta Bank in the model precludes an accurate representation of the coastal jets in the vicinity of NH-10, the model reasonably captures changes in direction of the coastal flow seasonally (Figure 2c).

## 4. Characteristics of the Slope Water

Given some reassurance that the model exhibits reasonable behavior both in the basin and on the shelf we now focus on describing the modeled means, trends, and variability for the slope waters. The general seasonal patterns are presented in the next section, followed by an analysis of the 26 year trends based on a linear fit. The last subsection focuses on interannual variability in slope water characteristics and the relative roles that coastal upwelling and California undercurrent strength play in determining it.

### 4.1. Seasonal Cycle

Prevailing winds in midlatitudes along the US west coast transition from northward, predominantly downwelling favorable, in winter, to southward, upwelling favorable, during the summer months. Fall and winter are characterized by strong wind mixing over the shelf and downward sloping isopycnals on the continental slope (Figure 3). While the spring and summer months see this pattern reverse with denser water shoaling onto the shelf and to the surface to form upwelling fronts. (Here winter is defined as December–February, spring as March–May, summer as June–August, and fall as September–November.) We present model results from a meridional section of frequent observational measurements, the Newport hydrographic line (NH-line,  $44.65^{\circ}\text{N}$ ,  $125^{\circ}\text{W}$ – $124.2^{\circ}\text{W}$ ), that is representative of the meridional structure across several degrees of latitude.

The downward displacement of isopycnals in winter over the outer shelf and slope is associated with a northward surface intensified jet. Oxygen levels are generally high as low-oxygen bottom waters are

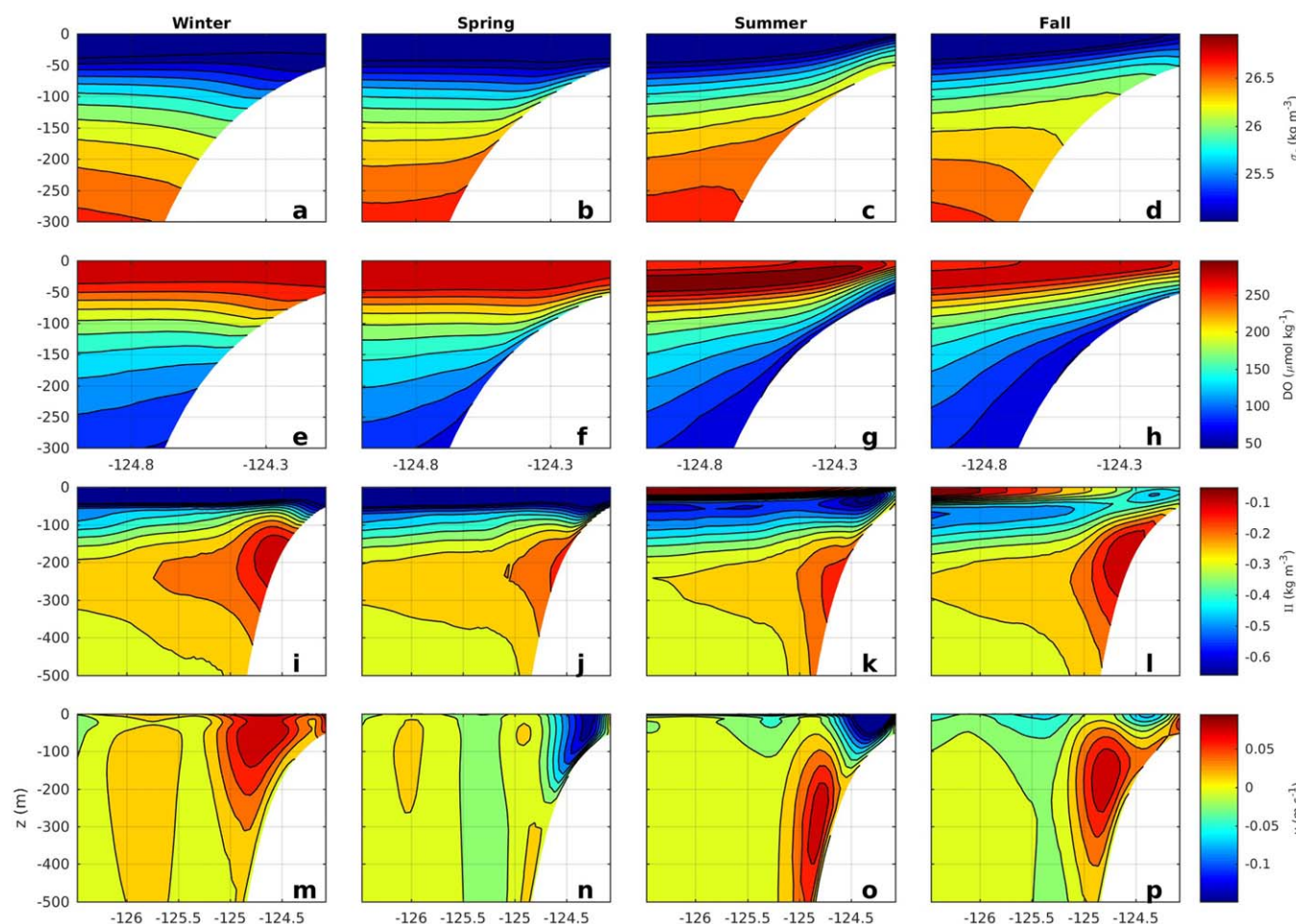


**Figure 3.** Seasonal averages of  $\sigma_\theta$  (top row), DO (second row), II (third row), and alongslope ( $v$ , poleward) velocity (bottom row) from the 26 year model simulation along the NH-line.

downwelled and strong wind mixing promotes atmospheric exchange. Surface cooling reduces the spiciness of surface waters while subsurface, northward flow advects higher spice water poleward.

The onset of the upwelling season occurs in spring. The upwelling front that results from the southward winds drives an equatorward surface intensified jet over the shelf (Figures 3b and 3n). The northward flow that persisted over the slope during winter is no longer present to advect warmer, saltier water poleward. This leads to springtime being the season with the lowest slope-water II of any season (Figure 3j). The oxycline generally mimics the pycnocline shoaling toward the coast and brings low DO waters onto the shelf (Figure 3f).

Summer is the peak upwelling season in the NCCS. Isopycnals shallower than about 250 m shoal over the slope and onto the shelf. In contrast to springtime, isolines of oxygen do not generally align with isopycnals in summer, as the influence of respiration in the lower part of the water column over the shelf and slope increases (Figure 3g). The biological aspects of oxygen dynamics also manifest as a subsurface DO maxima at the base of the mixed layer offshore of the upwelling front where photosynthesis acts as an oxygen source.

The poleward flowing undercurrent develops during summer. At the latitude of the NH-line, the model estimates an average summer core strength of approximately  $0.08 \text{ m s}^{-1}$  located approximately over the 500 m isobath between 200 and 300 m depth (Figure 3o). The upwelling jet is generally located shoreward and at shallower depths than the undercurrent, but model results indicate times when the two opposing currents are in proximity and may interact to attenuate each other. The pattern in spiciness reflects northward and shoreward advection over the slope.

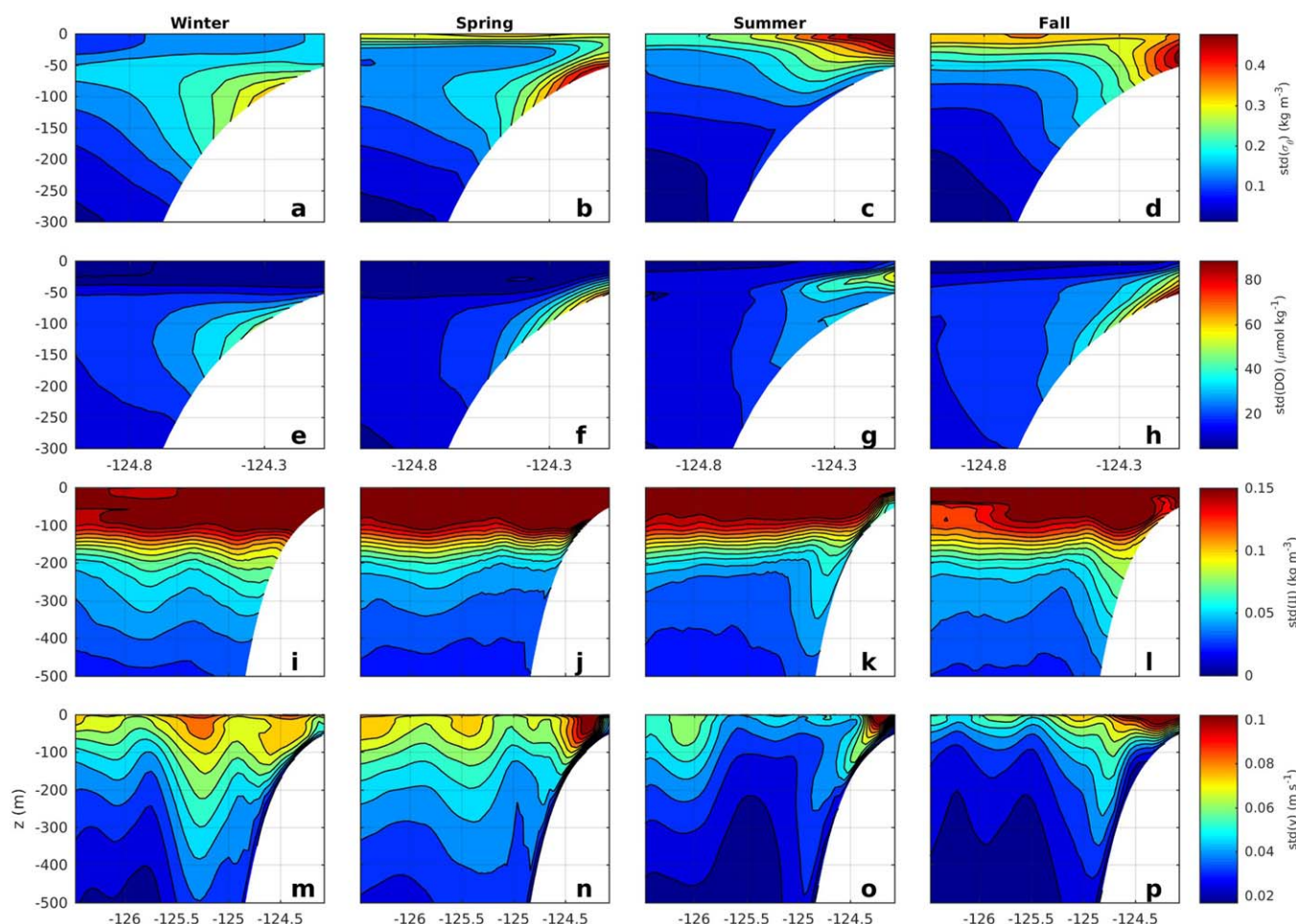


**Figure 4.** Standard deviation from monthly average fields of  $\sigma_\theta$ , DO,  $\pi$ , and alongslope (poleward) velocity from the 26 years of model simulation along the NH-line.

With the weakening of upwelling favorable winds by fall, the equatorward surface jet diminishes and the core of the undercurrent appears higher in the water column (Figure 3p). Spicy water is found far up on the slope and in the bottom waters of the shelf. Oxygen levels begin to recover and isopycnals relax.

Interannual variability in density is highest in frontal regions reflecting year-to-year variability in wind forcing (Figure 4, top row). In wintertime, variability is highest on the midshelf to outer-shelf, where downwelling isopycnals about the bottom. Density variance in spring is similar to winter but farther shoreward reflecting the transition to upwelling that brings dense bottom water shoreward. In summer, variability is surface intensified over the shelf consistent with the varying position of the upwelling front (Figure 4c) while fall variability reflects the relaxation of upwelling and upper ocean cooling as surface heat fluxes reverse sign.

In all seasons, the highest variability in oxygen concentrations is found subsurface, on the shelf. In winter, spring and fall variability is maximum near-bottom. In summer, variability is greatest on the midshelf to innershell in the midwater column at the base of the mixed layer, where respiration and photosynthesis rates are highest.

Velocity variability is surface intensified in all seasons (Figure 4, bottom row). In the spring, summer and fall it is largest in the region associated with the upwelling jet. Farther out on the slope, in winter and spring in particular, enhanced velocity variability is likely associated with eddy activity. While interannual variability in spiciness is dominated by variations in heating and cooling in the top 150 m, below this depth, variability is highest along the slope, particularly in fall and winter, coincident with the location of the undercurrent.



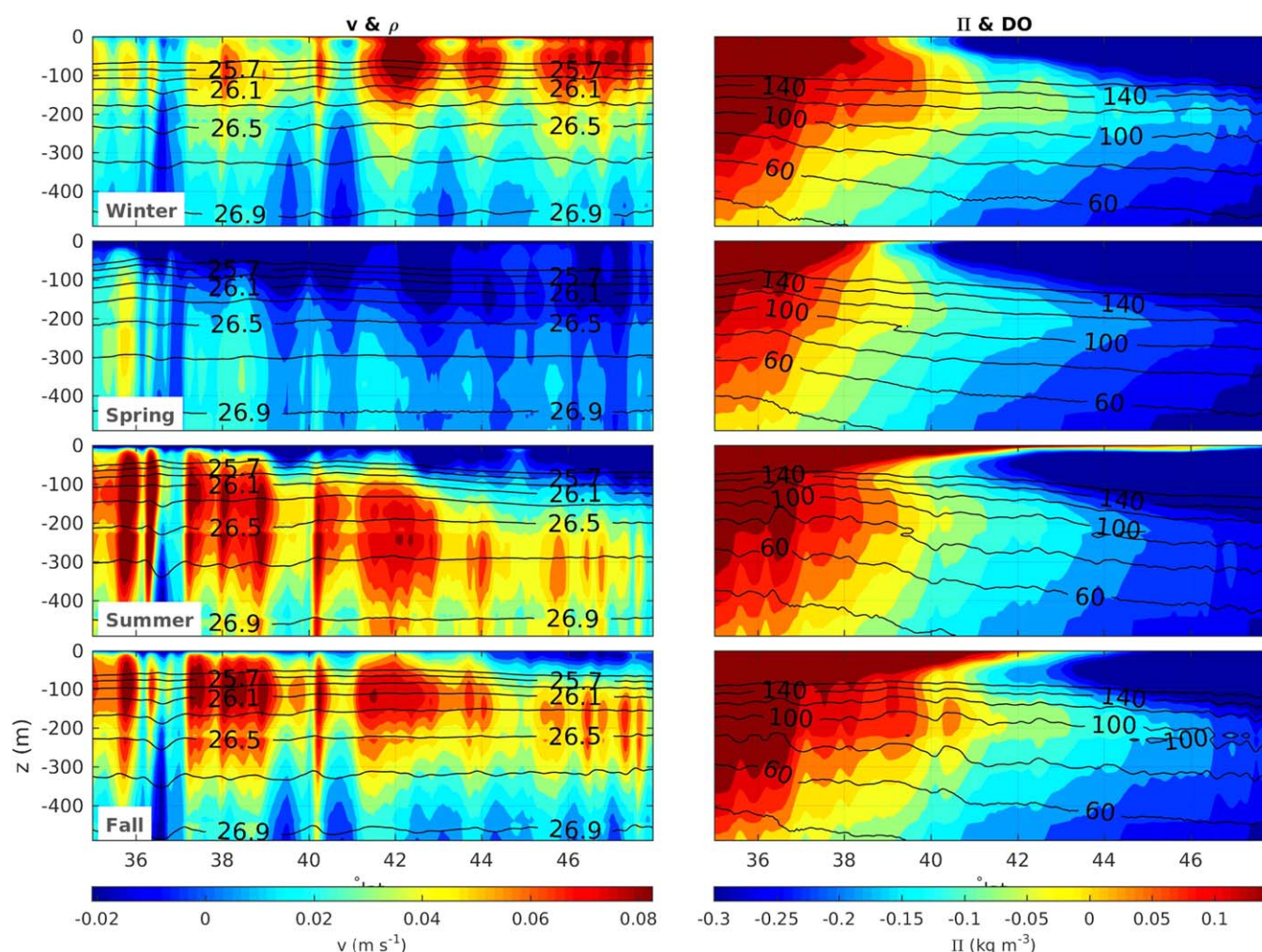


**Figure 5.** Seasonal average alongslope velocity and spiciness over the 500 m isobath as a function of latitude and depth.  $\sigma_\theta$  contours are overlaid on velocity in the left-hand plots. DO contours [mmol/m<sup>3</sup>] are overlaid on  $\Pi$  in the right-hand plots.

The long-term average seasonal cross-shore patterns depicted for the section at 44.65°N in Figure 3 are representative of meridional sections over much of the NCCS. Alongshore variability, in slope bathymetry, atmospheric forcing, and offshore source water properties, generally act to modify these patterns but not qualitatively alter them in the model. Alongslope structure is presented in Figure 5, as 26 year seasonal time-averaged fields, averaged spatially between the 1000 and 250 m isobaths. Latitudinal variation in wind forcing generally produces stronger northward winds in the northern portion of the model domain in winter, and stronger southward winds in summer in the southern portion of the model domain. This leads to a stronger surface intensified downwelling jet in winter, north of 41°N, and a stronger equatorward jet in spring, south of 43°N. The strongest upwelling favorable winds tend to shift northward from spring to summer in the California current system. Consequently the strongest equatorward surface intensified flows also shift farther north. The slope averaged alongslope velocity fields (Figure 5, left-hand plots) illustrate the seasonal evolution of the model-generated poleward undercurrent. The core of the undercurrent deepens from south to north, north of approximately 42°N (Figure 5). Density surfaces above approximately the  $\sigma_\theta = 26.5 \text{ kg m}^{-3}$  isopycnal (denoted  $\sigma_\theta^{26.5}$ ) do similarly. (This is consistent with the NCOM model results discussed by Connolly *et al.* [2014].) This deepening of the undercurrent core coincides with a weakening of the undercurrent strength. In the model, this develops beneath the region of intensified southward upwelling driven flow, suggesting that shear at the base of the upwelling jet attenuates flow in the upper portion of the undercurrent. Subsequently as upwelling relaxes in the NCCS in the fall, the average undercurrent core depth, north of 42°N, tends to move higher up the slope (also visible in Figures 3o and 3p).



The seasonal pattern in latitudinal distribution of spiciness reflects the variation in undercurrent and surface current strength and direction (Figure 5, right-hand plots). In the spring, flow over the slope is primarily southward in the upper 200 m of the water column and influenced by coastal downwelling, providing less-dense, colder, fresher subarctic water to the NCCS. This subarctic source water likely contributes to the poleward deepening of isopycnals that appears in the spring and summer. The development of the undercurrent however causes spicy equatorial source waters to be advected northward at depths below the southward flowing upwelling jet. This persists into fall and winter when the northward undercurrent transforms into a near-surface intensified flow. The modeled subsurface maximum in spice occurs at about 200 m depth in all seasons north of about 40°N, with the highest core spiciness at a given latitude occurring in fall or winter.

#### 4.2. Linear Trends

A number of observational studies have noted a long-term trend of increasing spiciness and decreasing DO of intermediate depth waters along the continental slope of the Northwest Pacific [Pierce *et al.*, 2012; Meinvielle and Johnson, 2013; Nam *et al.*, 2015]. The study of Pierce *et al.* [2012] focused on changes in water properties along the NH-line off the Oregon coast during summer (May–September), utilizing data collected between 1960 and 1971 and contrasting it with data collected along the same line between 1998 and 2009. They noted DO decreased strongly between  $\sigma_\theta = 27$  and  $\sigma_\theta = 26 \text{ kg m}^{-3}$  over the continental slope (analysis repeated here, Figure 6, top plots) between those periods. In the same data set, spiciness increased between the  $\sigma_\theta = 26.75 \text{ kg m}^{-3}$  isopycnal and the surface (Figure 6, bottom plots). Sampling the model along the same cross-shore transect and averaging over a 5 year period at the start of the simulation (1981–1985) and comparing with the last 5 years (2002–2006) suggests that the model results can also be interpreted as a positive trend in spiciness and negative trend in DO along isopycnals at intermediate depths on the slope. The strong positive trend in spiciness on the shallow isopycnals in the model may result from the lack of freshwater riverine input, as the model exhibits a much stronger positive trend in salinity than temperature on these isopycnals.

Meinvielle and Johnson [2013] analyzed historical data from the World Ocean Database between 25°N and 50°N and also found a trend of increasing spiciness and decreasing DO centered at depths characteristic of the core of the undercurrent. They attributed this to a strengthening of the undercurrent. Based on the observations, they determined that south of 40°N this was associated with a shoaling of isopycnals near the top of the undercurrent ( $\sigma_\theta = 26 \text{ kg m}^{-3}$ ) but that between 40°N and 45°N it was associated with a recession of isopycnals below the undercurrent (below 1000 m). We analyzed the linear trend in modeled average summertime (June–September) isopycnal depth for layers that generally enclose the core of the undercurrent ( $\sigma_\theta = 26$ – $27 \text{ kg m}^{-3}$ ). At the top of the undercurrent, on the slope, the  $\sigma_\theta = 26$  layer is found to shoal moderately over the 25 year simulation, at a rate of approximately  $0.25 \text{ m yr}^{-1}$ , while the  $\sigma_\theta = 27$  layer deepens at a similar rate (Figure 7). As suggested by Meinvielle and Johnson [2013], the net effect is a spreading of intermediate depth isopycnals on the slope. Based on this simulation, the  $\sigma_\theta = 26$  and  $\sigma_\theta = 27 \text{ kg m}^{-3}$  layers spread at a rate of approximately  $0.5 \text{ m yr}^{-1}$ .

Cross sections of linear trends in summer-averaged fields along the NH-line illustrate the long-term change in modeled slope water properties (Figure 8). At depths between 150 and 500 m, slope water spiciness is trending positively and DO negatively, consistent with an increased presence of waters coming from farther south. Density also tends to increase near-bottom between the 300 m isobath and the coast. But this is likely due to more frequent strong upwelling seasons in the later part of the simulation. One potential explanation for this pattern is that a strengthening of the California undercurrent leads to enhanced transport into the Oregon slope waters, however this is not borne out by the trend in northward velocity which shows a decrease for slope waters at all depths. Rather, the increased spiciness is associated with warmer saltier source waters to the south.

The time-averaged distribution of water properties within the domain at seven positions along the slope (Figure 9c) shows how water properties vary smoothly with latitude. To gain further insight into the degree to which alongshore transport is contributing to the large-scale model trend in intermediate depth water properties, fields can be scaled relative to their values at the northern and southern boundaries of the domain. The southern boundary water (SBW) can be considered representative of Pacific Equatorial source-waters while the northern boundary water (NBW) is indicative of North Pacific subarctic waters. Here the

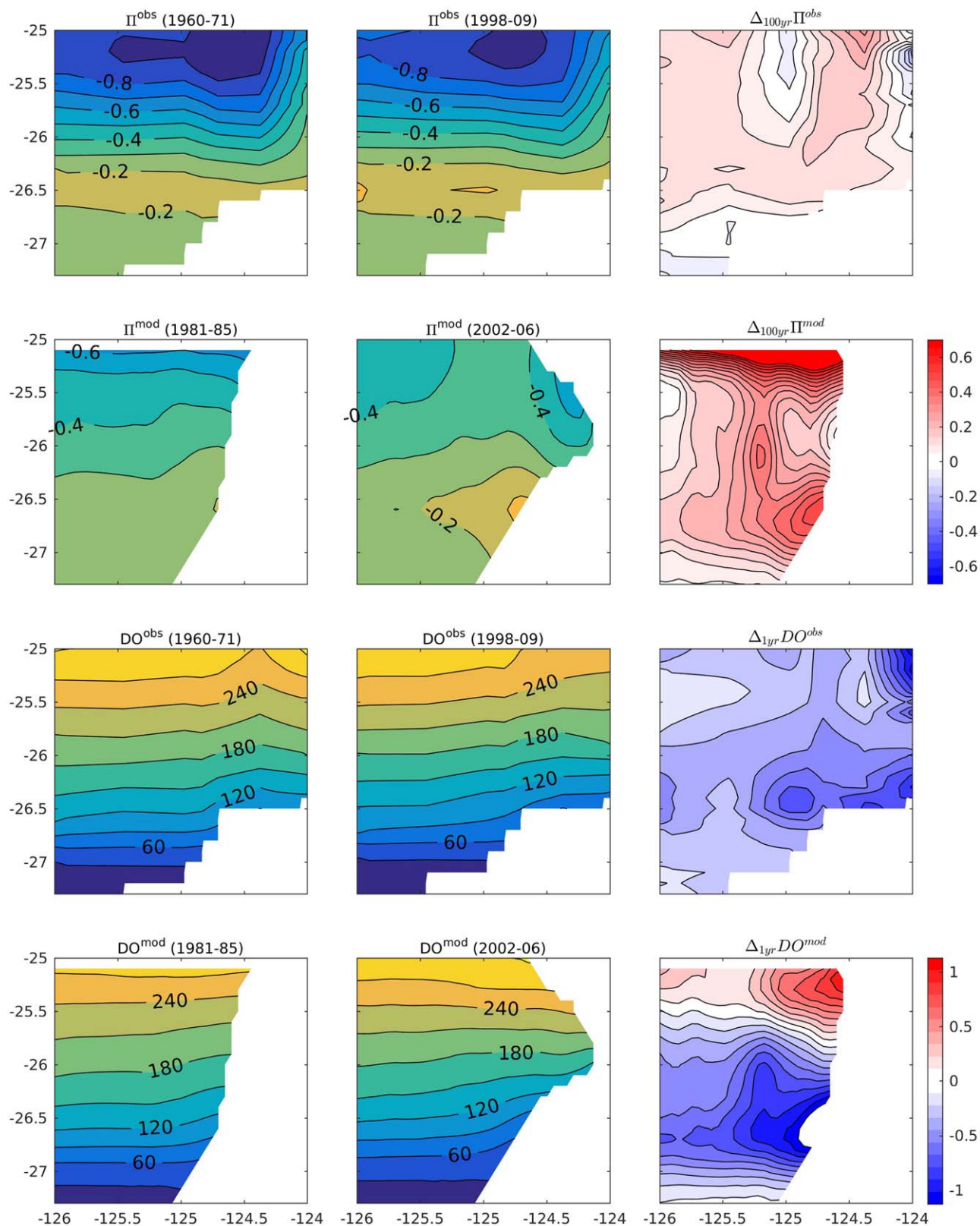


**Figure 6.** Comparison of trends in  $\pi$  and DO in observations and simulation along the NH-line. Observations are averaged over an early set of summer observations, 1960–1971 (leftmost), and a later set, 1998–2009. Similarly model is averaged over 1981–1985 and 2002–2006. Rightmost plots show the rate of change of the average fields in units of  $100 \text{ y}^{-1}$  for  $\pi$  and  $\text{y}^{-1}$  for DO.

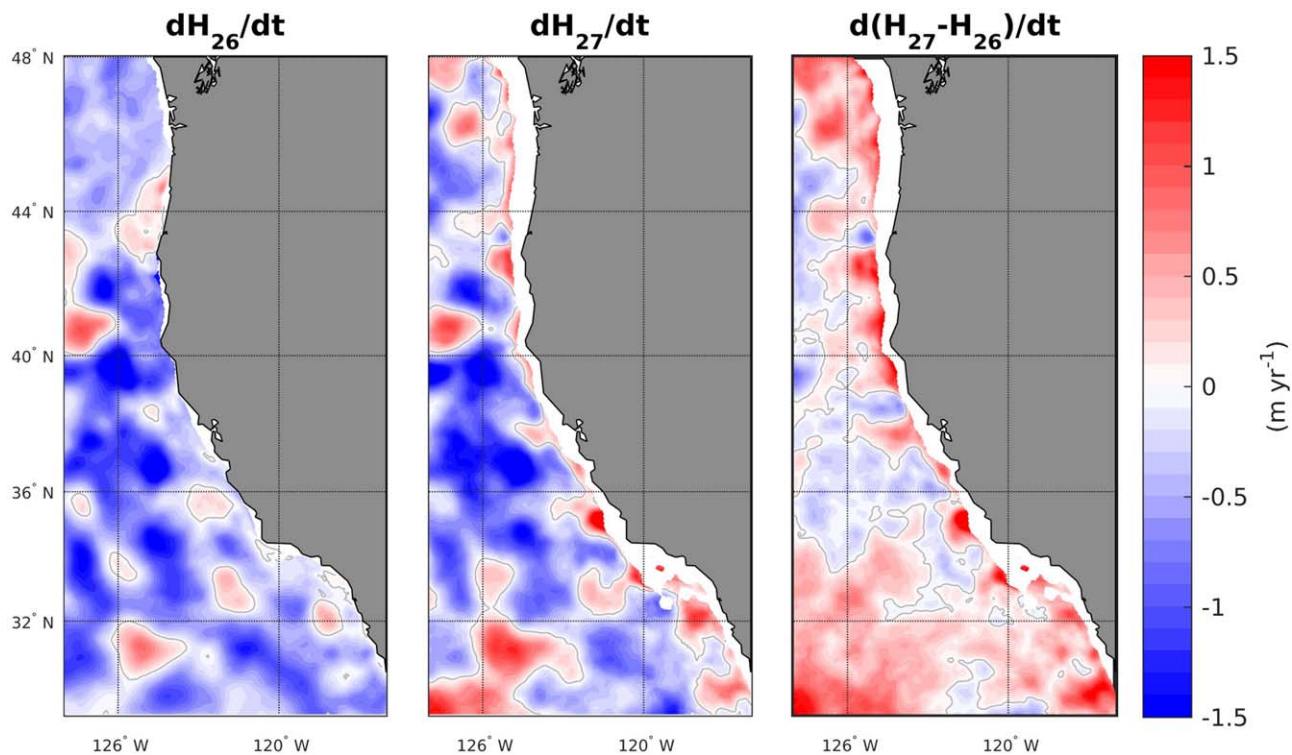


**Figure 7.** Plots display rate of change of isopycnal depth (measured from surface) for the (left)  $\sigma_\theta = 26$  and (middle)  $\sigma_\theta = 27$  layers and the rate of change of the intermediate layer thickness (right). The zero-contour is delineated with a gray line.

end-member properties for  $\Pi$  and DO are specified by first performing a linear fit (denoted  $\langle \rangle$ ) in time for each field at each grid point, and using these to estimate field values for September 1981. The SBW water ( $\Pi_{\text{SBW}}$ ,  $\text{DO}_{\text{SBW}}$ ) is identified as the water on the southern boundary with the highest value of  $\langle \Pi \rangle$  and lowest value of  $\langle \text{DO} \rangle$  (the slope water). Similarly the NBW ( $\Pi_{\text{NBW}}$ ,  $\text{DO}_{\text{NBW}}$ ) is specified as the water with the lowest  $\langle \Pi \rangle$ , and the  $\langle \text{DO} \rangle$  that occurs at the same location along the northern boundary (approximately 500 km offshore). The degree to which  $\sigma_\theta^{26.5}$  water is representative of the southern end-member, can then be estimated as,

$$\%_{\text{SBW}} \Pi(x, y, t) = \frac{\langle \Pi(x, y, t) \rangle - \Pi_{\text{SBW}}}{\Pi_{\text{NBW}} - \Pi_{\text{SBW}}} \quad (1)$$

For  $\Pi$  and similarly for DO. This normalized representation allows for comparison across the two fields.

The distribution of spiciness on  $\sigma_\theta^{26.5}$  results primarily from along isopycnal mixing of Pacific Equatorial Water entering the domain from the south and north pacific subarctic water entering the domain from the north. The spicy southern boundary water penetrates the domain most strongly along the shelf and slope. This leads to a  $\%_{\text{SBW}} \Pi$  distribution on  $\sigma_\theta^{26.5}$  that shows a gradual north-to-south gradient offshore, and a west-to-east gradient near the slope. The meridional gradient decreases from south to north as lateral mixing dilutes the water mass (Figure 9a).  $\%_{\text{SBW}} \text{DO}$  exhibits a similar west-to-east gradient indicative of the transport of low DO water from south to north in the California undercurrent (Figure 9b). The long-term linear trends in both  $\Pi$  and DO in the model on  $\sigma_\theta^{26.5}$  can be associated with the increasing influence of PEW and other factors. By normalizing both fields as a function of the end-member concentrations (noting that the end-member concentrations of neither field exhibit a significant long-term trend), one can compare the two to get an estimate of how much other processes may be playing a role in the evolution of each field. Between September 1981 and September 2006  $\Pi$  becomes approximately 10% more-like the southern end member over much of the domain (Figure 9d). DO on the other hand, while exhibiting a similar trend south of 36°N, shows a notably stronger trend north of this latitude (Figure 9e). The difference between the two fields (Figure 9f) gives a rough estimate of where the processes causing a trend in the biologically active



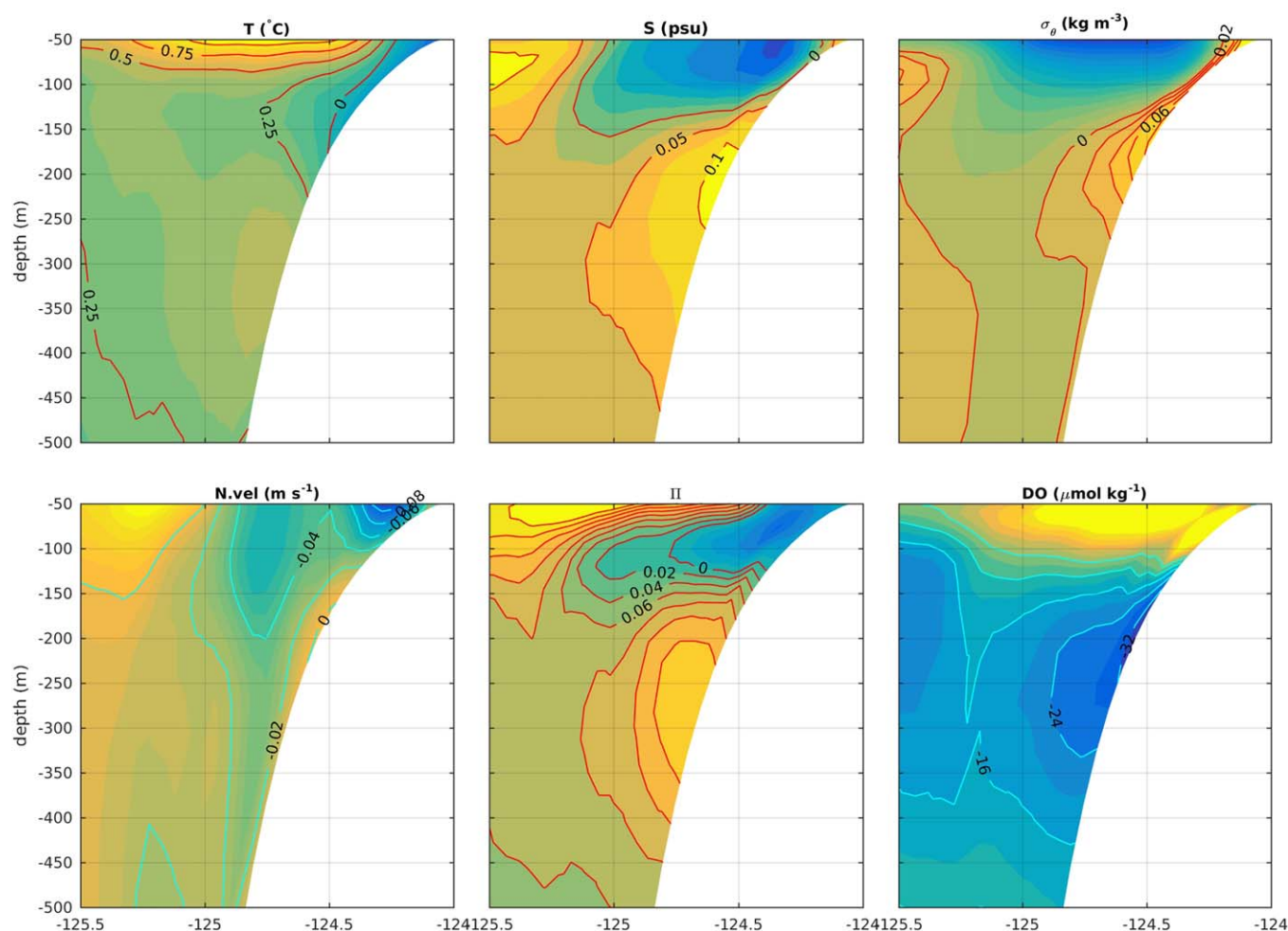


**Figure 8.** Linear trend in average September temperature, salinity, potential density anomaly, northward velocity, spiciness, and DO along the NH-line.

field (DO) differ from those causing a trend in a passive tracer field(II). Most likely these differences are associated with more oxygen-depleting biological processes north of 36°N although zonal differences in diapycnal mixing may also play a role.

### 4.3. Interannual Variability

The two features that predominantly determine the characteristics of the slope flow and shelf-slope interaction during summer and fall, are the coastal upwelling and the undercurrent. Here we attempt to classify each summer-fall season in terms of the intensity of these two features to distinguish characteristics of different forcing regimes. The intensity of upwelling is estimated based on the cumulative meridionally averaged (between 40°N and 47°N latitude), alongslope (equatorward) wind stress over the 250 m isobaths, integrated over an upwelling season. This follows the technique used by *Pierce et al.* [2006]. The undercurrent intensity is estimated based on the spatially averaged (between the 250 m isobaths and 1000 m isobaths and between 40°N and 47°N latitude), alongslope (northward-positive) velocity time-averaged over the upwelling season. In order to determine relative indices, each quantity is normalized by subtracting the time mean and dividing by its standard deviation. The 26 years of the simulation can then be classified into four categories based on whether the upwelling season conditions had anomalously strong or weak upwelling-favorable wind forcing (Upl'), and anomalously strong or weak undercurrent intensity (Ucl') (Figure 10). Grouping the years of the simulation in this way, yields 3 years with positive Upl' and positive Ucl' (referred to as Str/Str years), 8 years with positive Upl' but negative Ucl' (Str/Wk years), 6 years with positive Ucl' but negative Upl' (labeled Wk/Str), 8 years with both negative Upl' and negative Ucl' (Wk/Wk), and 1 year deemed too close to the mean of both indices to be categorized in one of the four classes. Throughout

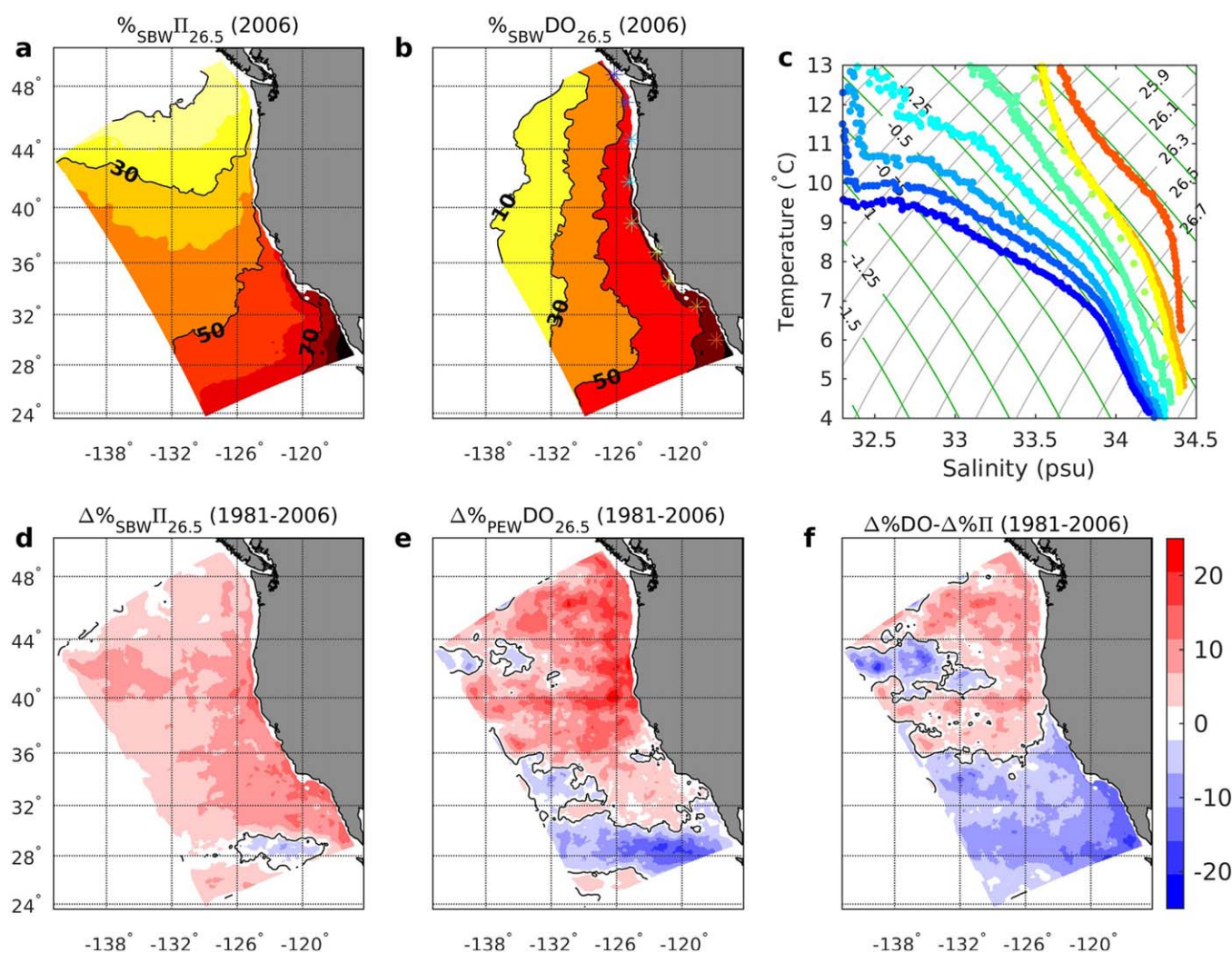


**Figure 9.** (a and b) Display contours of  $\%_{\text{SBW}} \Pi_{26.5}$  (Eq. 1) and  $\%_{\text{SBW}} \text{DO}_{26.5}$  on  $\sigma_{\theta}^{26.5}$  in September 2006, respectively. (c) T-S diagram of slope water properties at seven position within the model domain (colored to correspond with location labels in plots (b, d, and e) show the percent change in spiciness and DO on  $\sigma_{\theta}^{26.5}$  between September 1981 and September 2006. A positive percent change indicates a trend toward the southern end member. (f) The difference in the amount the percent end-member DO has changed relative to the amount the spiciness has changed.

the rest of this study these classifications will be used to identify how variability on the shelf, slope, and in the basin adjacent to the slope, is related to upwelling and undercurrent.

Strong undercurrent years ( $\text{Ucl}' > 0$ ) nearly always coincide with the onset of El Niño conditions (Figure 10c) in the Pacific as measured by the Multivariate ENSO index (MEI) [Wolter, 1987; Wolter and Timlin, 1993]. For example, the three upwelling seasons with the largest  $\text{Ucl}'$  are followed by the three winters with largest MEI over the 26 year time record. This correlation has been noted previously in observations focused on Baja and southern California [Ramp et al., 1997; Durazo and Baumgartner, 2002; Lynn and Bograd, 2002]. Frischknecht et al. [2015], using a telescopic Pacific biophysical model, to study the California Current System over the years 1979–2013, noted strong subsurface control of biogeochemical variables by remotely forced mechanisms (primarily coastally trapped waves associated with ENSO events) but mixed remote and local (primarily upwelling-favorable winds) control for surface fields.

In order to compare and contrast the influences of undercurrent strength and upwelling intensity, mean properties on a meridional slope section located along  $44.35^{\circ}\text{N}$  is examined first. (This section better represents the alongshore velocity structure than the  $44.65^{\circ}\text{N}$  section used above, which is in the lee of Heceta Bank.) September average fields are presented as they generally reflect the cumulative effect over the upwelling season for  $\sigma_{\theta}$ ,  $\Pi$ , and DO (Figure 11).

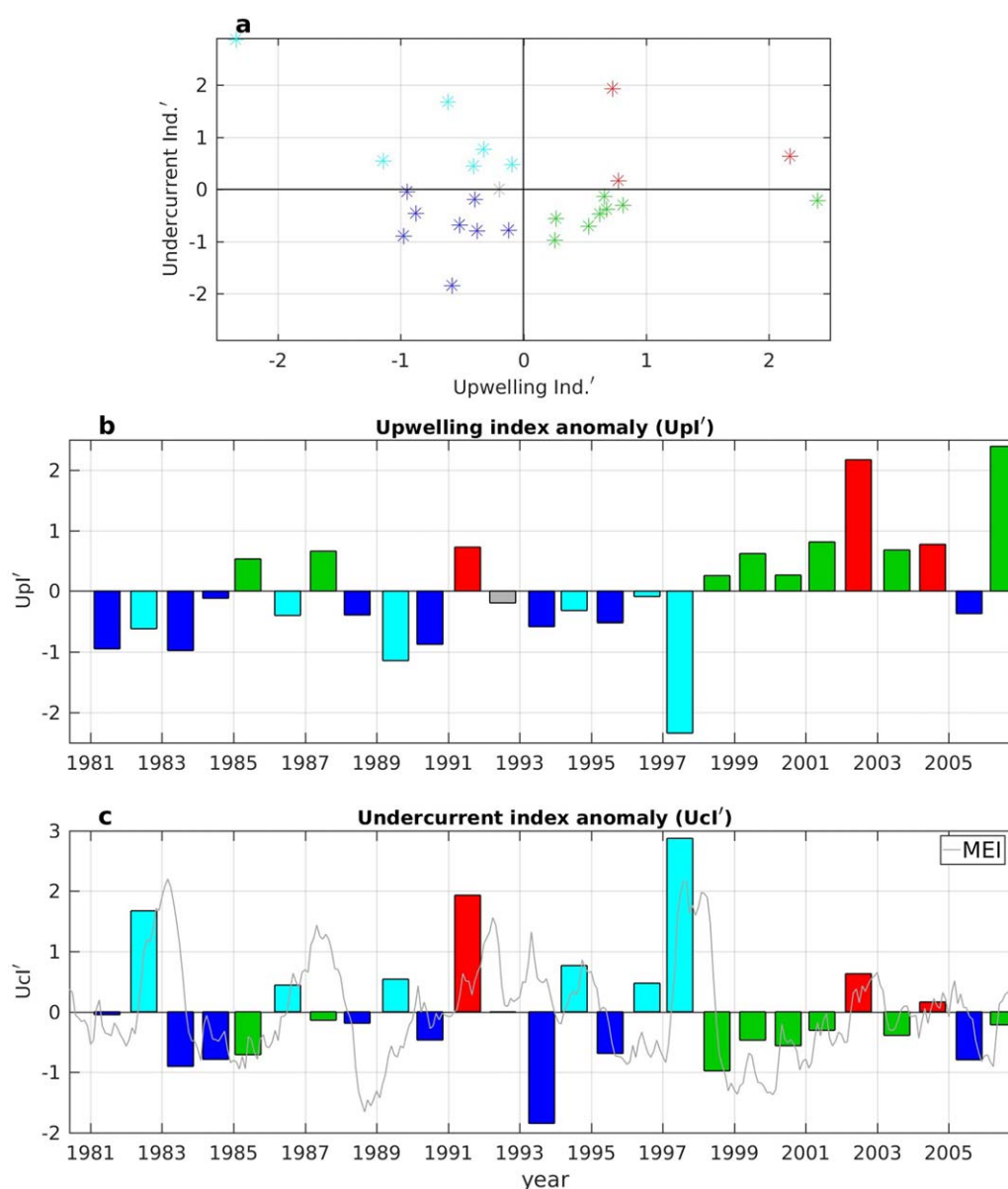


**Figure 10.** Classification of summer seasons in the NCCS. (a) displays a scatter plot of the 26 model years classified by cumulative upwelling and undercurrent strength relative to the 26 year mean values. (b) displays cumulative wind stress anomaly (through September) time series. (c) Displays cumulative undercurrent anomaly (through September) time series. Each year is colored based on the quadrant it falls into in the top plot. The multivariate ENSO index is overlaid in Figure 10c.

As can be anticipated, years with high Upl' and high Ucl' (Str/Str) in the NCCS, exhibit denser than normal shelf waters, with spicier, lower DO bottom water over the slope (first column of Figure 11).

Shoreward of the 150 m isobath, shelf DO is lowest in the years in which the upwelling tendency was strong but the undercurrent was weak (Str/Wk). This may simply be due to the upwelling index anomaly being on average not as strongly positive in the set of years with weak undercurrents as in the set of years with strong undercurrents (Figure 10), thus causing upwelling productivity to develop closer to shore. Alternately, low shelf DO in the Str/Wk years may result from enhanced nutrient supply to the shelf due to an increased influence of subarctic water intruding from the north as has been documented in observation of the Oregon shelf in 2002 [Wheeler et al., 2003]. Slope spiciness and DO characteristics in these years are near the 26 year average.

The model results suggest that a strong undercurrent in the absence of strong upwelling may tend to be broader and centered at a shallower depth (third column of Figure 11) and may tend to produce positive



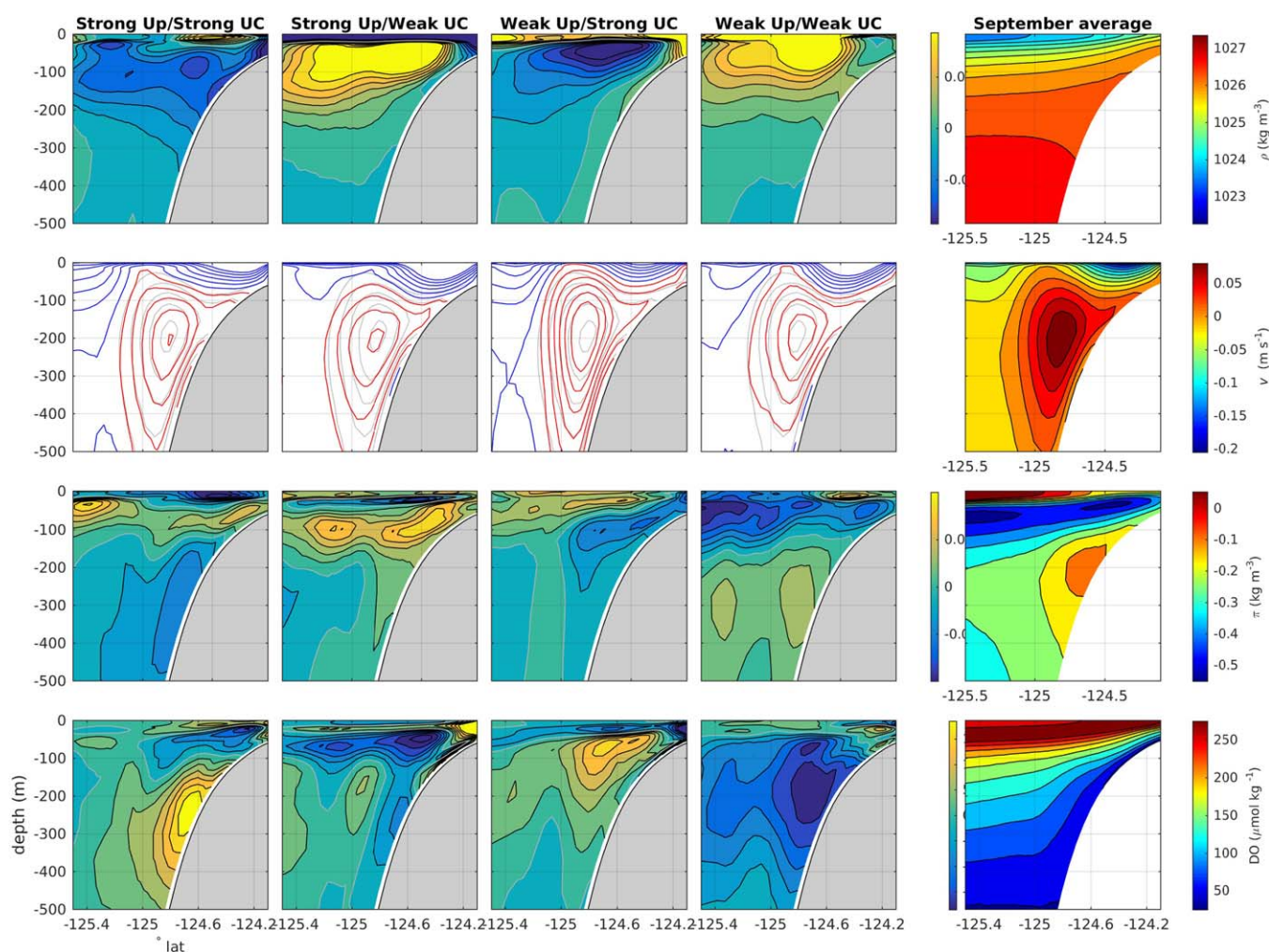


**Figure 11.** The first four columns display the average September anomaly in density, northward velocity, spiciness and DO at a meridional section at 44.35°N for the four sets of years classified as strong upwelling/strong undercurrent, strong upwelling/weak undercurrent, weak upwelling/strong undercurrent and weak upwelling/weak undercurrent. The rightmost plots display the 26 year August average of each field. Velocity panes in the second row, display contours every  $0.02 \text{ m s}^{-1}$  with northward contours in red and southward contours in blue. Gray contours in the second row of contour plots indicate the 26 year average undercurrent position. Gray contours in other plots indicate the zero contour.

anomalies in spice and negative anomalies in DO over deeper slope isobaths. When both the undercurrent and the upwelling are weak, the lack of northward transport of spicy, low DO water, over the slope results in higher than average DO and lower than average spice, while the reduction in shelf productivity leads to higher than average bottom shelf water DO.

The higher primary productivity that develops in the spring and early summer mixed layers over the slope in strong upwelling years can be associated with enhanced respiration and declining DO concentrations deeper in the water column. In the model simulation, anomalously low DO is found in the undercurrent waters in years with anomalously strong upwelling favorable forcing (Figure 12). Here the undercurrent is identified as anomalously spicy northward flowing middepth slope water. The anomaly ( $\text{DO}'$ ) is calculated as the difference at a given point in a given month averaged over the set of years in a particular class, from the 26 year average DO at that point in that month. In years with both strong upwelling and a strong undercurrent the model suggests a northward propagation of negative  $\text{DO}'$  with continuing drawdown due to respiration into October. The apparent propagation of a positive  $\text{DO}'$  anomaly in Figure 12 in years with weak upwelling and weak undercurrent likely indicates that the average year exhibits some propagation of a negative anomaly. In general, the anomaly in undercurrent DO approaches zero by January of the following year.

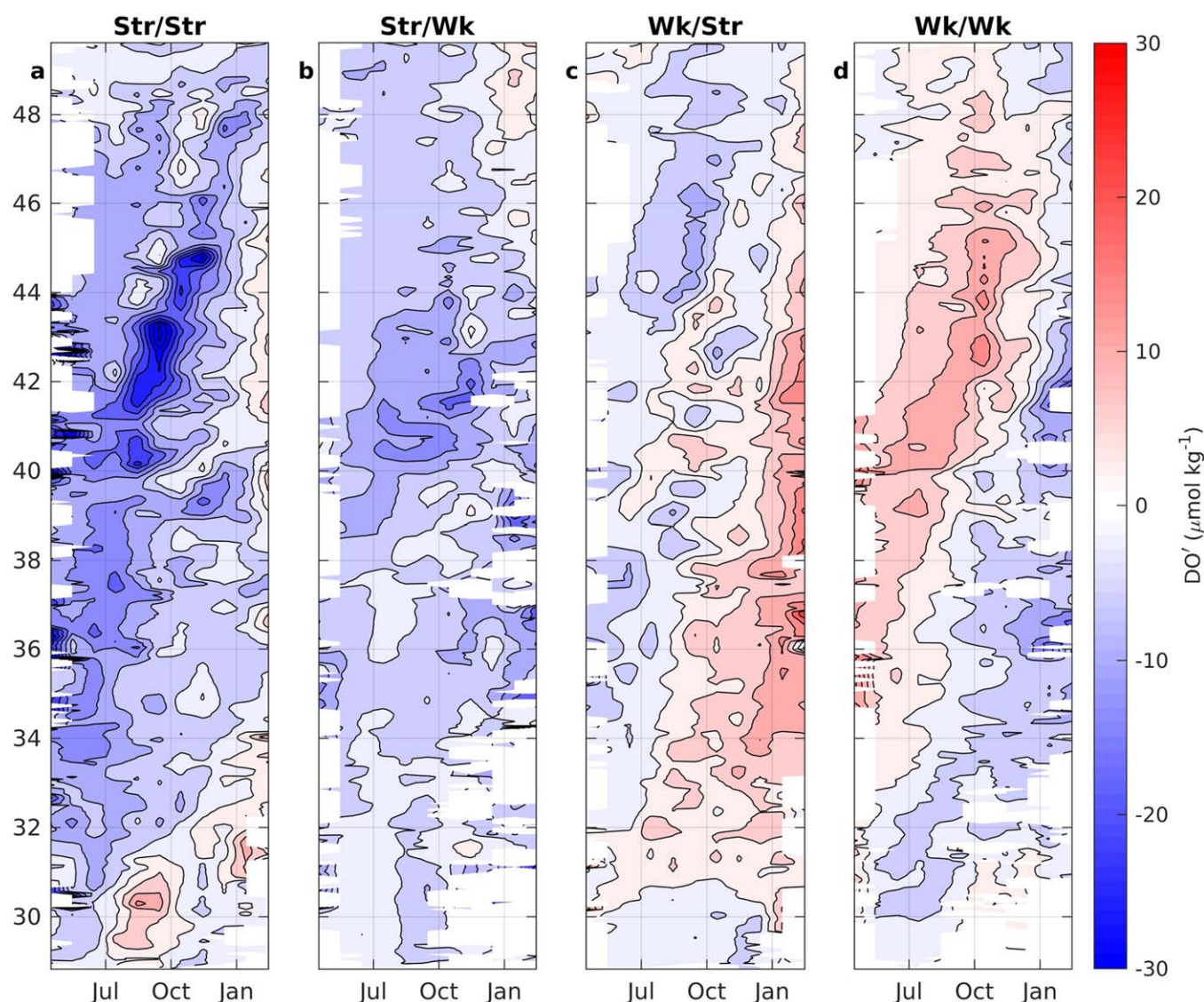


**Figure 12.** Average undercurrent DO anomaly as a function of latitude and time for the four classes of years. Time axes run from mid-May to mid-March of the following year. Gaps indicate times and locations that did not exhibit a well-defined northward flowing anomalously spicy middepth slope flow.

## 5. Slope-Shelf Exchange

During the upwelling season, slope water from beneath the surface boundary layer advects shoreward, while in strong downwelling seasons shelf water may be transported onto the upper slope. The seasonal patterns in shelf-slope exchange of near-bottom water are reflected in DO and spiciness, and vary with upwelling and undercurrent intensities (Figures 13 and 14). The seasonal patterns can be more easily interpreted with consideration of the average winter conditions that preceded and followed each of the classes of years. Table 1 shows the average anomaly in downwelling favorable wind stress and surface heat flux during the winter seasons. This average is estimated from the model forcing as the average along the 250 m isobaths between 40°N and 47°N latitude. The starts and ends of each winter season are specified as the complimentary periods to the upwelling periods defined above such that the “downwelling anomaly, prior year” reflects the net northward wind stress over the period beginning with the end of the upwelling season of the previous year and ending with the beginning of the upwelling season of a given year. The winter properties assumed for the winter of 1980–1981 and winter 2006–2007 are assumed to be the 26 year averages.



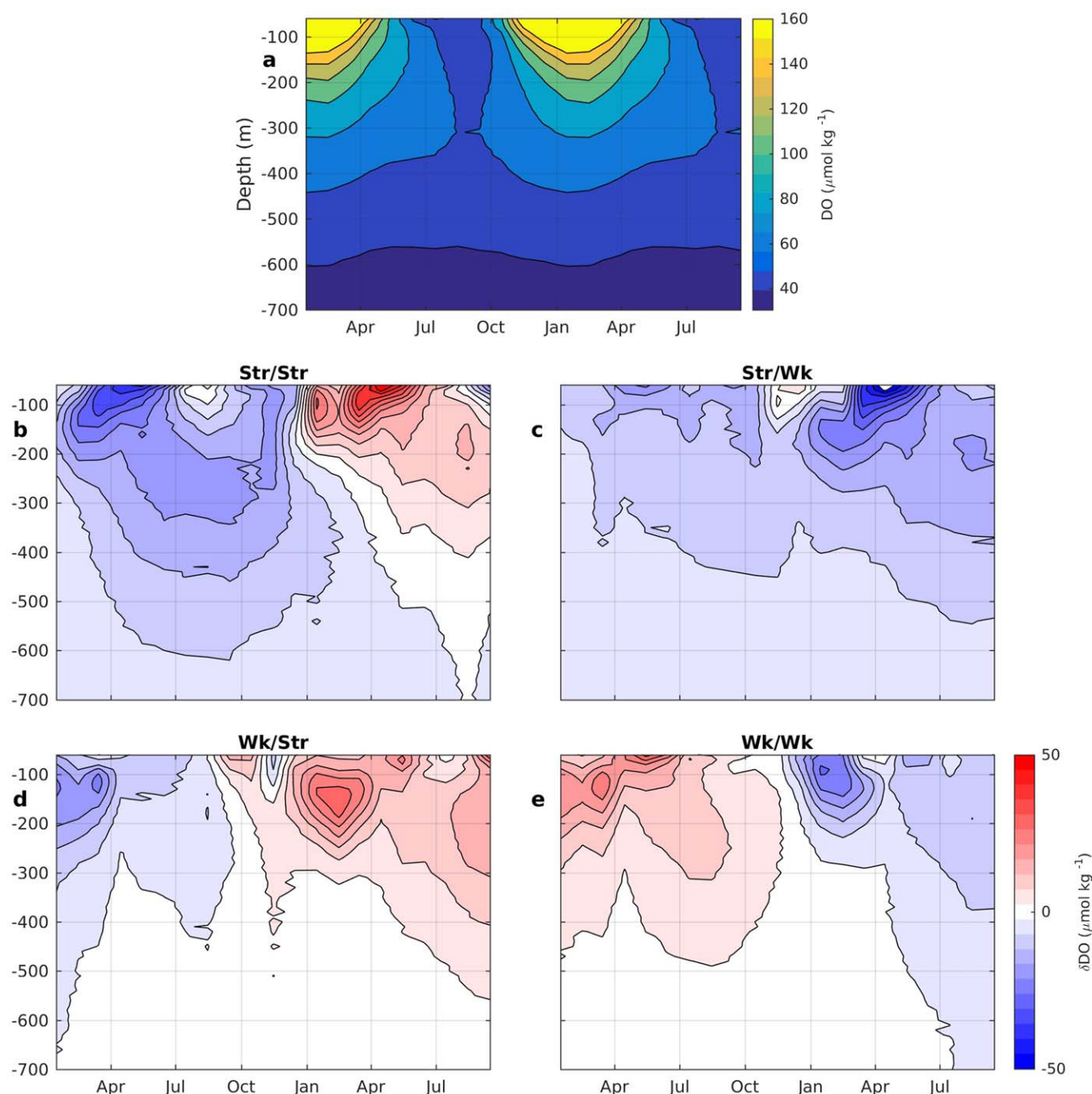


**Figure 13.** (a) 26 year average near-bottom DO, averaged latitudinally along isobaths, contoured as a function of month. Plots (b–e) display the DO anomaly from this seasonal average for the four classes of years. Time axes extend 9 months into the following year.

The 26 year average cycle of near-bottom DO on the shelf and upper slope exhibits a seasonal pattern of highest DO in winter and lowest DO in mid-to-late summer (Figure 13a). The annual maximum on the shelf and slope is produced by vigorous vertical mixing on the shelf resulting from generally stronger winter winds and surface cooling. As winter winds tend to be downwelling favorable, these highly oxygenated waters tend to be transported off shelf, down the slope roughly between October and March. As surface winds reverse to upwelling favorable, lower DO water is drawn back onto the shelf causing shelf and upper slope DO to start to decline on average in March of each year. During the summer, as productivity is enhanced in the upper water column by the upwelling, shelf bottom respiration increases. Concurrently,



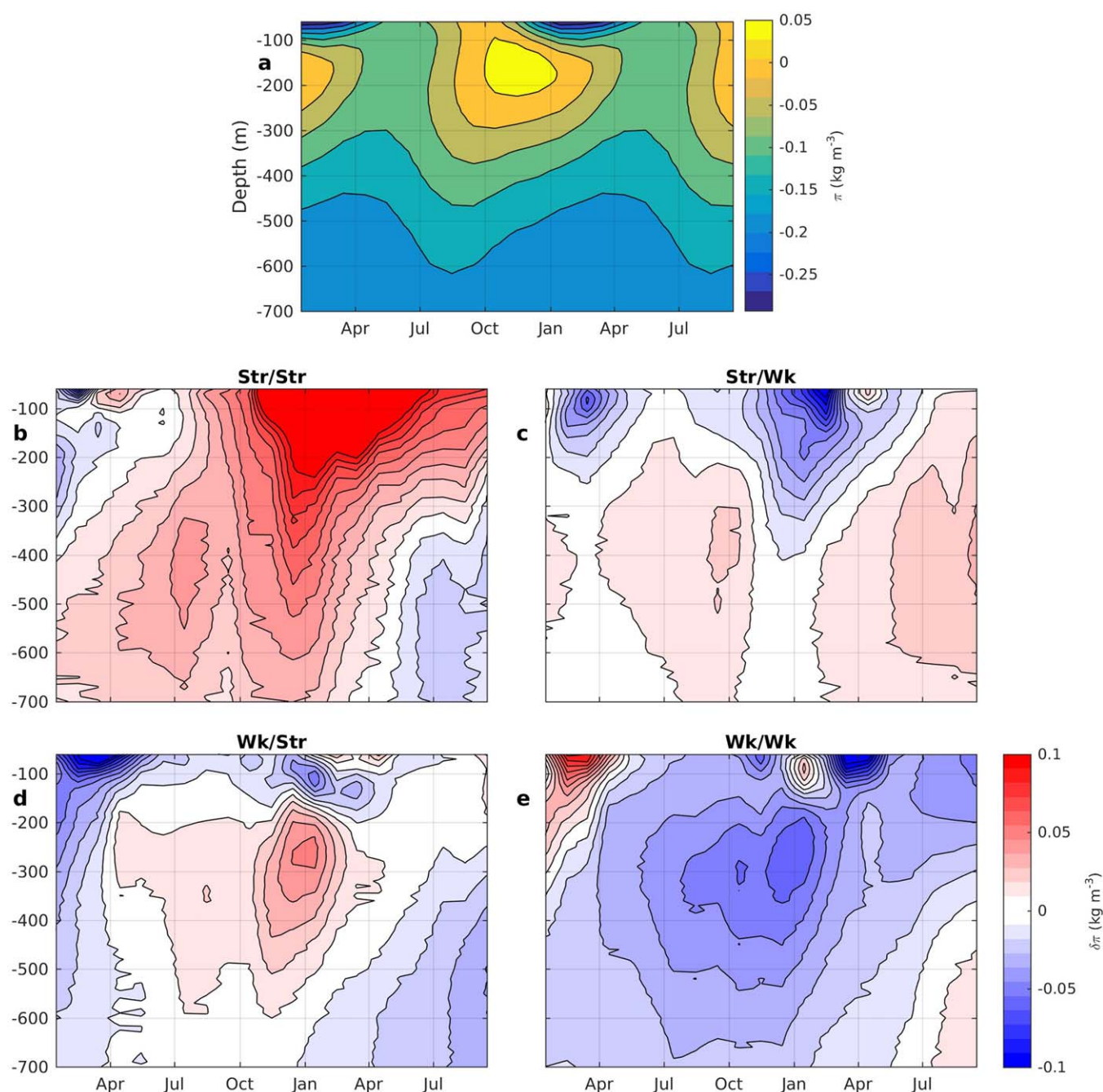


**Figure 14.** (a) Seasonal average near-bottom  $\pi$ , averaged along slope and shelf isobaths. Plots (b–e) display the spiciness anomaly from this seasonal average for the four classes of years.

the undercurrent develops. These processes jointly contribute to shelf and slope bottom DO reaching a minimum on average in late summer to early fall. On average, this seasonal cycle affects bottom DO above the 500 m isobath.

Considering the anomalies to this pattern under the set of four upwelling/undercurrent conditions outlaid above confirms some expected consequences (Figures 13b–13e). Stronger upwelling seasons lead to a negative anomaly in shelf bottom water DO and weaker seasons can lead to a positive summer-fall anomaly. The effect of a strong undercurrent during strongly upwelling years is a lower than average slope bottom DO between 200 and 600 m. But during weakly upwelling years this leads to a lesser depression of slope

**Table 1.** Average Winter Downwelling Anomalies and Winter Surface Heat Flux Anomalies for Prior and Subsequent Years for Years in the Four Classes of Upwelling and Undercurrent Intensities<sup>a</sup>

	Str/Str	Str/Wk	Wk/Str	Wk/Wk
Downwelling anomaly, prior winter	−0.32	0.2	−0.12	0.04
SHF anomaly, prior winter	−63	−166	73	44
Downwelling anomaly, following winter	0.05	−0.13	0.4	−0.16
SHF anomaly, following winter	967	−136	−185	−177

<sup>a</sup>Downwelling anomaly is in  $\text{N m}^{-2}$ . Surface heat flux anomaly (SHF) is in units of  $\text{Watts m}^{-2}$ .

bottom water DO (consistent with Figure 12). Tabulating the average number of days, in a given upwelling season, of hypoxic conditions on the shelf (75 m isobaths, averaged between 40°N and 47°N latitude) and slope (250 m isobaths) also illustrates this point (Table 2). While the average number of days of hypoxia ( $\text{DO} < 64 \mu\text{mol kg}^{-1}$ ) on the shelf is nearly identical for the Str/Str and Str/Wk cases, the average number

of days of slope hypoxia is much greater in the Str/Str case. This may relate to the intensity of the prior downwelling seasons as discussed below.

In three of the four classes (Str/Str, Wk/Str, Wk/Wk), anomalies that develop in the bottom water of the shelf and upper slope in one upwelling season do not persist through the winter into the next spring. Interestingly however, the intensity of winter downwelling can have an impact on the persistence of an anomaly well into the upwelling season, or in the case of strong upwelling/weak undercurrent years, through the winter months. The downwelling anomalies for prior and subsequent years presented in Table 1 show that the years with strong upwelling and strong undercurrents were preceded by some of the weakest downwelling winters while the years with strong upwelling and weak undercurrents were preceded by some of the strongest downwelling winters. As a result the negative anomaly in bottom shelf and upper slope DO in spring in the Str/Str case is notably larger than in the Str/Wk case. The average of the Wk/Wk years, which are preceded by stronger than average downwelling favorable winds exhibit a positive DO anomaly on the shelf and upper slope throughout the upwelling season. The effect of downwelling in the subsequent winters in each of the cases is also apparent, as the Str/Str and Wk/Str cases exhibit positive DO anomalies into the following years, with stronger than average winter downwelling. The Str/Wk and Wk/Wk years tend to produce negative anomalies into the following year with weaker than average downwelling winds.

The seasonal cycle in shelf and slope near-bottom spice (Figure 14) indicates the effects of the summer strengthening of the undercurrent, the transition to the Davidson current in fall/winter and the seasonal heating and cooling cycles on the shelf. Maximum shelf and slope spiciness occurs in October with the spiciest water tending to lie above the 175 m isobaths. Spice drops to an annual minimum on the shelf in February, due to both downwelling and cooling. On the slope the minimum occurs somewhat later in April–May, perhaps due to off-shelf eddy transport (explored in next section).

Comparison of the four combinations of upwelling/undercurrent intensities demonstrates, as expected, that slope water is more spicy in late summer, fall, and winter when the undercurrent is strong and less spicy when the undercurrent is weak. Strong upwelling can lead to a moderate positive anomaly in slope spice even when the undercurrent is weak by elevating near-bottom slope isopycnals. However, a significant portion of the anomalies in spice are not directly related to the intensity of the upwelling and undercurrent as the particulars of the winter forcing contribute significantly. The net winter surface heat flux (Table 1) can vary greatly. The three winters following years with strong upwelling and strong undercurrents were forced with particularly strong positive (into the ocean) anomalies in surface heat flux. The positive near-bottom spice anomaly that results extends beneath the 700 m isobaths. The winters following Str/Wk, Wk/Str, and

Wk/Wk summer seasons all show negative anomalies in surface heat flux and fresh anomalies in spice on the shelf but with differing anomalies on the slope. The Wk/Str set of years, that shows positive slope bottom-water spice anomalies in the subsequent winter, includes the 2 years in which the onset of strong El Niño events occurred (1982, 1997). Interestingly, these two years exhibited the strongest undercurrents of the 26 year series.

**Table 2.** Anomaly in Number of Days of Latitudinally Averaged (40°N and 47°N Latitude) Hypoxic Conditions ( $< 64 \mu\text{mol kg}^{-1}$ ) in the Bottom Water of the Shelf (75 m Isobath) and Slope (250 m Isobath) for the Four Classes of Upwelling/Undercurrent Intensities<sup>a</sup>

	Str/Str	Str/Wk	Wk/Str	Wk/Wk
Slope Bot.	96	26	−2	−48
Shelf Bot. Hyp.	31	33	−13	−28

<sup>a</sup>Negative anomalies mean that many days fewer than the average number of days hypoxia during the upwelling season.

## 6. Slope-Basin Exchange

Slope exchange with the north Pacific basin can occur as eddies associated with coastal jets or with the undercurrent are shed into the interior. These eddies tend to be most abundant during the fall transition at the end of the upwelling season. At this time, it is typical for  $\sigma_{\theta}^{26.5}$  to be sloped upward while the  $\sigma_{\theta} = 27.0 \text{ kg m}^{-3}$  isopycnal is level or depressed in the simulation. The band of slope water in between the two tends to be higher in  $\Pi$  and lower in DO compared to the water offshore at the same latitude. By examining the average properties between these two levels and the vertical thickness of this layer ( $\Delta H_{\text{iso}}$ ) we see that, not surprisingly, the eddies often manifest as regions of positive anomaly in  $\Delta H_{\text{iso}}$ , positive anomalies in  $\Pi$ , and negative anomalies in DO. As an example, anomaly fields for October 1985 are presented in Figure 15 at the end of a season with strong upwelling but a relatively weak undercurrent.

Eddy abundance varies seasonally as does the concentration of  $\Pi$  and DO advected with them. In order to quantify these patterns, variances and correlations are calculated for spatially high-pass filtered ( $\sim O[300 \text{ km}]$ ) model fields. The high-pass filtered field variances and correlations are averaged between  $40^{\circ}\text{N}$  and  $47^{\circ}\text{N}$  latitude and between  $129^{\circ}\text{W}$  and the 1500 m isobath. Fields are averaged over each month for the full 26 year simulation and for each set of years of different upwelling and undercurrent intensities. The variation in layer thickness west of the undercurrent is generally at a minimum in April of each year and at a maximum around October (Figure 16a) when isopycnals that have upwelled over the summer tend to relax. During the first half of the year, in the region immediately offshore of the slope, variance in  $\Pi$  and DO diminish as eddies from the previous fall and winter dissipate. While in the latter half of the year, they tend to increase as the upwelling and undercurrent begin to shed eddies with anomalous water properties

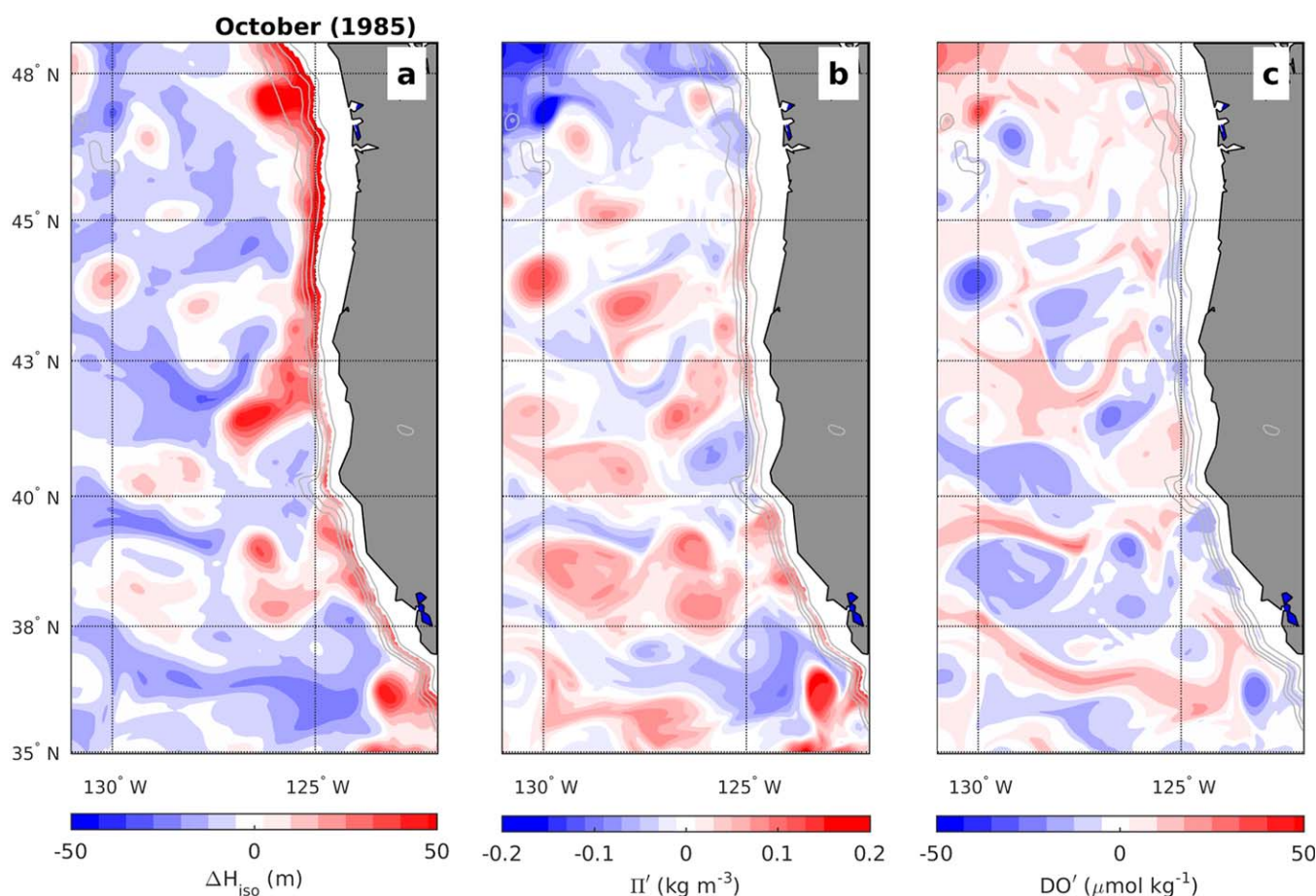


**Figure 15.** (a) The anomaly in thickness of the layer delineated by the  $\sigma_{\theta} = 26.5$  and  $27.0 \text{ kg m}^{-3}$  isopycnals. (b and c) The anomaly in layer-averaged  $\sigma_{\theta}$  and DO, respectively. Gray contour lines indicate isobaths between  $-2000 \text{ m}$  and  $-500 \text{ m}$  at a  $500 \text{ m}$  interval.



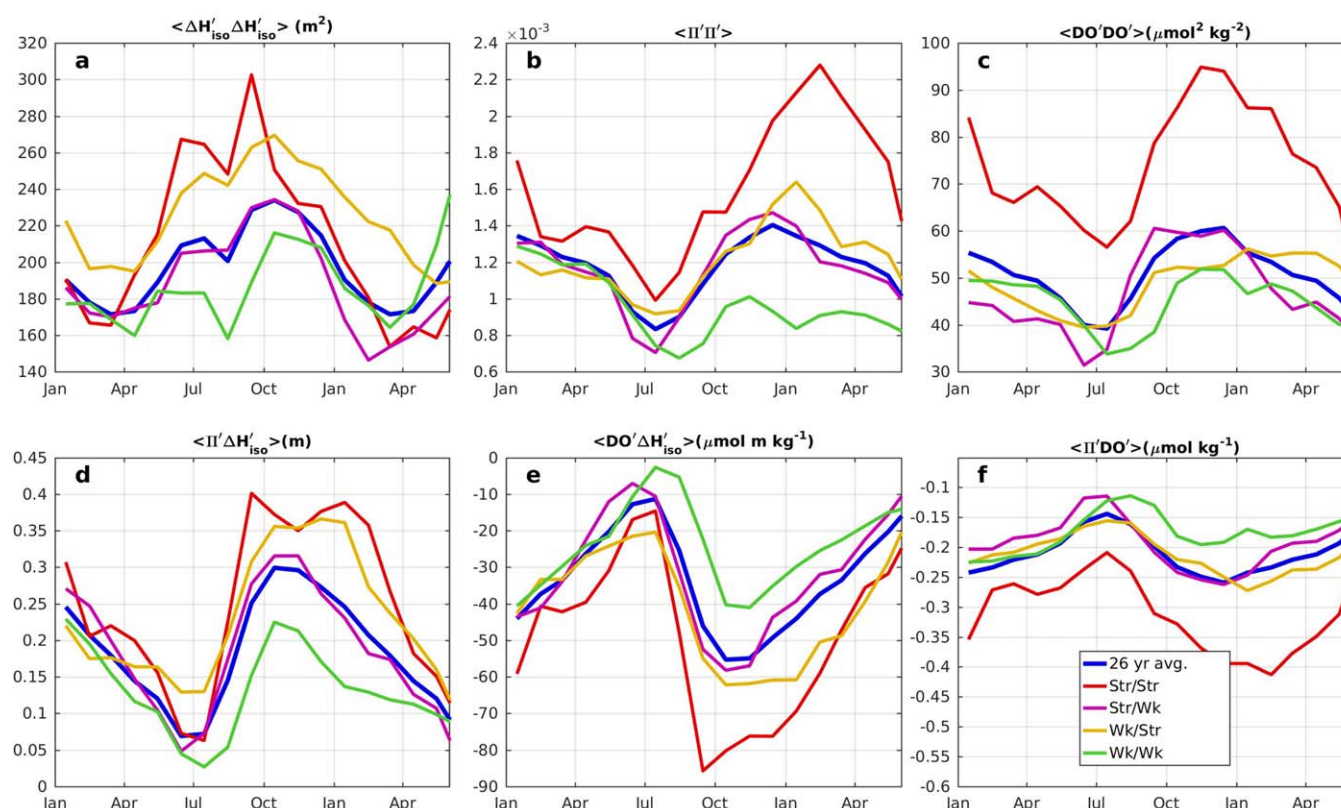


**Figure 16.** Spatially averaged anomaly field variances and covariances averaged by month, for the full 26 year simulation and separately for years in each of the four classes of upwelling and undercurrent intensities. Fields are averaged between 40°N and 47°N latitude and between 129°W and the 1500 m isobaths.  $\Delta H_{iso}$  is the anomaly in thickness between the  $\sigma_\theta = 26.5$  and  $27.0 \text{ kg m}^{-3}$  isopycnal.  $\Pi'$  and  $DO'$  are anomalies from the layer average in  $\Pi$  and  $DO$ , respectively.

westward (Figures 16b and 16c). As is the case in Figure 15, anomalously thick regions of this layer are correlated with anomalously spicy water and low DO throughout the entire year and vice versa for thin regions.

Comparison of the seasonal cycles in these correlations for years in the four classes of upwelling and undercurrent intensities suggests that years with strong upwelling and strong undercurrents have the largest impact on variability offshore and this impact is particularly large in the late summer and early fall. Conversely, Wk/Wk years lead to the smallest fall increases in variability in the neighboring portion of the North Pacific basin. Since the average correlation between  $\Delta H_{iso}$  and  $DO$  is negative one can conclude that on average the offshore subthermocline environment exhibits the greatest negative  $DO$  anomalies in October and the lowest  $DO$  years are ones in which both strong upwelling and a strong undercurrent develops.

## 7. Discussion

A 26 year biophysical simulation of the region of the North Pacific adjacent to the US west coast has been analyzed to examine the characteristics of and variability in slope-water characteristics in the NCCS. The model reproduces a northward flowing undercurrent that intensifies in late summer, merges with the northward flowing, surface-intensified Davidson Current in winter, and diminishes in the spring of each year. The large scale, south-to-north gradients of decreasing spice and increasing  $DO$ , result in the undercurrent transports being characterized by anomalously high spice and low  $DO$  at a given latitude particularly in late summer and early fall.

Slope water characteristics could be expected to remain relatively consistent from year-to-year if there are compensatory processes that decrease spice and reoxygenate the slope water column. Downwelling and deep vertical mixing in the winter is one such mechanism which reintroduces colder and fresher, oxygen-rich waters to the upper slope. Transport of fresh, high-oxygen subarctic water southward in the upwelling

jet is another that acts counter to the influence of the undercurrent. Eddy-shedding by the undercurrent that diminishes the northward transport can be a moderating process as well.

Nonetheless an analysis of the linear trends in spice and DO over the 26 years of the simulation (1980–2006) suggests that slope water spice increased and DO decreased consistent with the findings of several previous observational studies over this period. The model results exhibit a quantitatively consistent trend in spice and DO in the Southern California Current System suggestive that both are dictated by increased net advection of equatorial source waters (as suggested in the literature). But in the NCCS the trend in DO is much stronger than in spice, implying that biological dynamics are also being altered over time. Recent studies that extend to years prior to and after the period simulated here, suggest that what is interpreted as a long-term trend in observations of DO in the CCS over these years, is more appropriately described as decadal variability [Crawford and Pena, 2016; Pozo Buil and Di Lorenzo, 2017]. But no attempt is made here to extrapolate beyond the simulated years.

While over longer time scales decadal scale variability may interfere with the detection of a linear long-term trend, it is important to note that there is very significant year-to-year variability in slope water characteristics as well. A sequence of years in which the winds are anomalously upwelling favorable and/or the undercurrent is anomalously strong toward the end of a time series could mimic the effect of a linear trend. In order to better understand the interplay between winds, undercurrent, shelf, and slope dynamics, a portion of this study was devoted to examining the seasonal to interannual influences of undercurrent and upwelling intensity.

Upwelling seasons with uncharacteristically strong upwelling favorable winds and undercurrent intensity, not surprisingly, tend to exhibit the strongest anomalies in slope spice and DO. Strong upwelling acts to raise isopycnals on the upper slope, reducing the DO and increasing the spiciness at a given depth. Concurrently a strong undercurrent acts to transport high spice, low DO water northward. Anomalies were not nearly as strong in years with either one of these elements missing.

Anomalies in undercurrent DO were shown to propagate northward over the upwelling season. In both years with intense upwelling and undercurrent or weak upwelling and undercurrent the deviation from mean undercurrent DO that develop in the southern portion of the domain propagate northward (with speeds between 0.04 and 0.09 m s<sup>-1</sup>). Given the spring onset of the upwelling season in the southern California Current system and the limited rate of northward transport, latitudes between approximately 39°N and 42°N are likely the most vulnerable to hypoxic conditions in the slope water due to the combined effect of undercurrent transport and local upwelling. North of these latitudes, undercurrent-transported low DO water is not likely to arrive until the fall, when upwelling processes are waning.

Observational studies have noted anomalously low shelf bottom water DO on the Oregon coast both in 2002 and in 2006. Whereas in 2006 this is generally perceived to be associated with particularly strong upwelling favorable winds, 2002 exhibited (and 2006 did not) an unusual intrusion of relatively fresh, high-nutrient content, halocline, subarctic water from the north [Wheeler *et al.*, 2003]. The model reproduces a comparable level of shelf hypoxia in both years by September despite the Upl' being significantly larger in 2006. Although it is difficult to determine if increased nutrient loading supplied to the shelf from the subarctic water in 2002 contributed to the hypoxia, as the observations of the intrusion were made in July, and the model shows the presence of fresh oxygen rich halocline water on the shelf in July, it is worth considering that there are multiple pathways to similarly anomalous conditions.

Whether or not the bottom water characteristics from one upwelling season carry over into the next spring depends as much on the conditions in the intervening winter as on the intensity of the upwelling and undercurrent during the upwelling. In some instances, where winter downwelling forcing was weak, slope bottom water DO anomalies persisted through the winter and contributed to the characteristics of the water upwelled in the spring. But in other cases, the shelf and slope anomalies that developed during the upwelling season dissipated under strong winter forcing both on the shelf and on the slope. Anomalies in spice, on the other hand, tended to intensify over the winter months of strong downwelling seasons as more spicy upper undercurrent water advected north in merged downwelling jets and undercurrent flow. Whereas changes in spice and DO tended to be negatively correlated on the slope in summer, in winter, they tended to be positively correlated as the process that led to higher spice is associated with deeper mixing of well oxygenated surface waters.

Processes on the slope affect the intermediate water properties in the adjacent open ocean mostly through eddy-mixing processes. Years with strong undercurrents tend to produce more offshore eddy activity in the NCCS. In years with strong upwelling as well, these eddies tended to be characterized by anomalously high spice and low DO. Although the average offshore conditions were not quantified in this study, it is clear that the intensity of the processes on the slope and shelf will determine the degree of heterogeneity in the open ocean intermediate water adjacent to the slope. Typically this heterogeneity peaks in October and gradually diminishes over the winter and following spring.

This study focused on the general slope water characteristics in the NCCS with the primary goal of developing an understanding of the source water DO variability that might contribute to the development of shelf bottom water hypoxic conditions during the upwelling season. While the moderate horizontal resolution used here allowed for drawing broad conclusions about the seasonal patterns and alongshore-averaged interchange between shelf and slope, in many years, regions of hypoxic conditions are likely to be more spatially and temporally localized.

To further advance our understanding in this area, future studies will need to better resolve the biogeochemical and bathymetric details of shelf and slope while maintaining a faithful representation of the remotely forced variability in the California Undercurrent and California Current system in general. Extending simulations such as this one into more recent years that have been sampled more extensively will help resolve questions of interannual and decadal variability versus trends.

# Acknowledgments

This work was supported by funding from the Gordon and Betty Moore Foundation (GBMF#3775), the David and Lucile Packard Foundation, the National Science Foundation (OCE-1419323), and the National Oceanic and Atmospheric Administration (NA15NOS4780186). Oregon NH-10 mooring data were made available thanks to the NANOOS project and efforts by M. Kosro, M. Levine, and C. Risien. Dissolved oxygen data for the Newport hydrographic line were kindly provided by S. Pierce. Argo and SODA data set are available from the Asia-Pacific Data-Research Center (APDRC) at the University of Hawaii (<http://apdrc.soest.hawaii.edu/data/data.php>). The NARR data set is available from NOAA National Centers for Environmental Information (<https://www.ncdc.noaa.gov/data-access/model-data/model-datasets/north-american-regional-reanalysis-narr>).

# References

- Argo (2000), Argo float data and metadata from Global Data Assembly Centre (Argo GDAC), SEANOE. [Available at <http://doi.org/10.17882/42182>.]
- Armstrong, R. A., C. Lee, J. I. Hedges, S. Honjo, and S. G. Wakeham (2002), A new, mechanistic model for organic carbon fluxes in the ocean based on the quantitative association of POC with ballast minerals, *Deep Sea Res., Part II*, 49(1–3), 219–236, doi:10.1016/S0967-0645(01)00101-1.
- Bograd, S. J., C. G. Castro, E. Di Lorenzo, D. M. Palacios, H. Bailey, W. Gilly, and F. P. Chavez (2008), Oxygen declines and the shoaling of the hypoxic boundary in the California Current, *Geophys. Res. Lett.*, 35, L12607, doi:10.1029/2008GL034185.
- Carton, J. A., G. Chepurin, X. Cao, and B. S. Giese (2000a) A Simple Ocean Data Assimilation analysis of the global upper ocean 1950–1995, Part 1: Methodology, *J. Phys. Oceanogr.*, 30, 294–309.
- Chelton, D. B. (1984), Seasonal variability of alongshore geostrophic velocity off central California, *J. Geophys. Res.*, 89(C3), 3473–3486, doi:10.1029/JC089iC03p03473.
- Connolly, T. P., B. M. Hickey, I. Shulman and R. E. Thomson (2014), Coastal trapped waves, alongshore pressure gradients, and the California undercurrent, *J. Phys. Oceanogr.*, 44, 319–342, doi:10.1175/JPO-D-13-095.1.
- Crawford, W. R., and M. A. Peña (2013) Declining oxygen on the British Columbia continental shelf, *Atmos. Ocean*, 51(1), 88–103, doi:10.1080/07055900.2012.753028.
- Crawford, W. R., and M. A. Peña (2016), Decadal trends in oxygen concentration in subsurface waters of the Northeast Pacific Ocean, *Atmos. Ocean*, 54(2), 171–192, doi:10.1080/07055900.2016.1158145.
- Deutsch, C., H. Brix, T. Ito, H. Frenzel, and L. Thompson (2011), Climate-forced variability of ocean hypoxia, *Science*, 33(6040), 336–339, doi:10.1126/science.1202422.
- Durazo, R., and T. R. Baumgartner (2002), Evolution of oceanographic conditions off Baja California 1997–1999, *Prog. Oceanogr.*, 54(1–4), 7–31, doi:10.1016/S0079-6611(02)00041-1.
- Frischknecht, M., M. Münnich, and N. Gruber (2015), Remote versus local influence of ENSO on the California Current System, *J. Geophys. Res. Oceans*, 120, 1353–1374, doi:10.1002/2014JC010531.
- Garcia, H. E., R. A. Locarnini, T. P. Boyer, J. I. Antonov, M. M. Zweng, O. K. Baranova, and D. R. Johnson (2010a), World Ocean Atlas 2009, in *Nutrients (Phosphate, Nitrate, Silicate)*, NOAA Atlas NESDIS 71, vol. 4, edited by S. Levitus, 398 pp., U.S. Gov. Print. Off., Washington, D. C.
- Garcia, H. E., R. A. Locarnini, T. P. Boyer, J. I. Antonov, O. K. Baranova, M. M. Zweng, and D. R. Johnson (2010b), World Ocean Atlas 2009, in *Dissolved Oxygen, Apparent Oxygen Utilization, and Oxygen Saturation*, NOAA Atlas NESDIS 70, vol. 3, edited by S. Levitus, 344 pp., U.S. Gov. Print. Off., Washington, D. C.
- Gruber, N., H. Frenzel, S. C. Doney, P. Marchesiello, J. C. McWilliams, J. R. Moisan, J. Oram, G. K. Plattner, and K. D. Stolzenbach (2006), Eddy-resolving simulations of plankton ecosystem dynamics in the California Current System, Part I: Model description, evaluation, and ecosystem structure, *Deep Sea Res., Part I*, 53, 1483–1516, doi:10.1016/j.dsr.2006.06.005.
- Hales, B., L. Karp-Boss, A. Perlin, and P. A. Wheeler (2006), Oxygen production and carbon sequestration in an upwelling coastal margin, *Global Biogeochem. Cycles*, 20, GB3001, doi:10.1029/2005GB002517.
- Huyer, A., J. A. Barth, P. M. Kosro, R. K. Shearman, and R. L. Smith (1998), Upper-ocean water mass characteristics of the California Current, summer 1993, *Deep Sea Res., Part II*, 45, 1411–1442.
- Key, R. M., A. Kozyr, C. L. Sabine, K. Lee, R. Wanninkhof, J. L. Bullister, R. A. Feely, F. J. Millero, C. Mordy, and T.-H. Peng (2004), A global ocean carbon climatology: Results from Global Data Analysis Project (GLODAP), *Global Biogeochem. Cycles*, 18, GB4031, doi:10.1029/2004GB002247.
- Lynn, R., and S. Bograd (2002), Dynamic evolution of the 1997–1999 El Niño-La Nina cycle in the southern California Current System, *Prog. Oceanogr.*, 54(1–4), 59–75, doi:10.1016/S0079-6611(02)00043-5.
- Marchesiello, P., J. C. McWilliams, and A. Shchepetkin (2003), Equilibrium structure and dynamics of the California Current System, *J. Phys. Oceanogr.*, 33, 753–783, doi:10.1175/1520-0485.
- McClatchie, S., R. Goericke, R. Cosgrove, G. Auad, and R. Vetter (2010), Oxygen in the Southern California Bight: Multidecadal trends and implications for demersal fisheries, *Geophys. Res. Lett.*, 37, L19602, doi:10.1029/2010GL044497.



- Meinvielle, M., and G. C. Johnson (2013), Decadal water-property trends in the California Undercurrent, with implications for ocean acidification, *J. Geophys. Res. Oceans*, *118*, 6687–6703, doi:10.1002/2013JC009299.
- Mesinger, F., et al. (2006), North American regional reanalysis, *Bull. Amer. Meteor. Soc.*, *87*, 343–360, doi:10.1175/BAMS-87-3-343.
- Moore, J. K., S. C. Doney, and K. Lindsay (2004), Upper ocean ecosystem dynamics and iron cycling in a global three-dimensional model, *Global Biogeochem. Cycles*, *18*, GB4028, doi:10.1029/2004GB002220.
- Nam, S., Y. Takashita, and C. Frieder (2015), Seasonal advection of Pacific Equatorial Water alters oxygen and pH in the Southern California Bight, *J. Geophys. Res.*, *120*, 5387–5399, doi:10.1002/2015JC010859.
- Pelland, N. A., C. C. Eriksen, and C. M. Lee (2013), Subthermocline eddies over the Washington continental slope as observed by Seagliders, 2003–09, *J. Phys. Oceanogr.*, *43*, 2025–2053.
- Pierce, S. D., R. L. Smith, P. M. Kosro, J. A. Barth, and C. D. Wilson (2000), Continuity of the poleward undercurrent along the eastern boundary of the mid-latitude north Pacific, *Deep Sea Res., Part II*, *47*, 811–829, doi:10.1016/S0967-0645(99)00128-9.
- Pierce, S. D., J. A. Barth, R. E. Thomas, and G. W. Fleischer (2006), Anomalously warm July 2005 in the northern California Current: Historical context and the significance of cumulative wind stress, *Geophys. Res. Lett.*, *33*, L22S04, doi:10.1029/2006GL027149.
- Pierce, S. D., J. A. Barth, R. K. Shearman, and A. Y. Erofeev (2012), Declining oxygen in the Northeast Pacific, *J. Phys. Oceanogr.*, *42*(3), 495–501, doi:10.1175/JPO-D-11-0170.1.
- Pozo Buil, M., and E. Di Lorenzo (2017), Decadal dynamics and predictability of oxygen and subsurface tracers in the California Current System, *Geophys. Res. Lett.*, *44*, 4204–4213, doi:10.1002/2017GL072931.
- Ramp, S. R., J. L. McClean, C. A. Collins, A. J. Semtner, and K. A. S. Hays (1997), Observations and modeling of the 1991–1992 El Niño signal off central California, *J. Geophys. Res.*, *102*(C3), 5553–5582, doi:10.1029/96JC03050.
- Shchepetkin, A. F., and J. C. McWilliams (2005), The Regional Ocean Modeling System: A split-explicit, free-surface, topography following coordinates ocean model, *Ocean Modell.*, *9*, 347–404.
- Thomson, R. E., and M. V. Krassovski (2010), Poleward reach of the California Undercurrent extension, *J. Geophys. Res.*, *115*, C09027, doi:10.1029/2010JC006280.
- Wheeler, P. A., A. Huyer and J. Fleischbein (2003), Cold halocline, increased nutrients and higher chlorophyll off Oregon in 2002, *Geophys. Res. Lett.*, *30*(15), 8021, doi:10.1029/2003GL017395.
- Wolter, K. (1987), The Southern Oscillation in surface circulation and climate over the tropical Atlantic, Eastern Pacific, and Indian Oceans as captured by cluster analysis, *J. Clim. Appl. Meteorol.*, *26*, 540–558.
- Wolter, K., and M. S. Timlin (1993), Monitoring ENSO in COADS with a seasonally adjusted principal component index, in *Proceedings of the 17th Climate Diagnostics Workshop, Norman, OK*, pp. 52–57, NOAA/NMC/CAC, NSSL, Oklahoma Clim. Surv., CIMMS and the Sch. of Meteorol., Univ. of Oklahoma, Okla.

## Erratum

In the originally published version of this article, Crawford, W. R. et al. (2016) was missing from the reference list. This has since been corrected and this version may be considered the authoritative version of record.

In the originally published version of this article, Figure 11 was incorrect. The correction to figure have since been made to the online version only, which may be considered the authoritative version.